



รายงานวิจัยฉบับสมบูรณ์

โครงการ

การประยุกต์ใช้วงจรกรองโวลเทอราสำหรับภาพจากอัลตราซาวน์แบบไม่เชิงเส้น

Applications of Volterra Filters for Nonlinear Ultrasound Imaging

โดย ผู้ช่วยศาสตราจารย์ ดร. พรชัย พฤกษ์ภัทรานนต์

เดือน ปี ที่เสร็จโครงการ กรกฎาคม 2552

รายงานวิจัยฉบับสมบูรณ์

โครงการ

*การ*ประยุกต์ใช้วงจรกรองโวลเทอราสำหรับภาพจากอัลตราซาวน์แบบไม่เชิงเส้น

Applications of Volterra Filters for Nonlinear Ultrasound Imaging

โดย ผู้ช่วยศาสตราจารย์ ดร. พรชัย พฤกษ์ภัทรานนต์ ภาควิชาวิศวกรรมไฟฟ้า คณะวิศวกรรมศาสตร์ มหาวิทยาลัยสงขลานครินทร์

สนับสนุนโดยสำนักงานคณะกรรมการการอุดมศึกษา และสำนักงานกองทุนสนับสนุนการวิจัย (ความเห็นในรายงานนี้เป็นของผู้วิจัย สกอ. และ สกว. ไม่จำเป็นต้องเห็นด้วยเสมอไป)

บทคัดย่อ

รหัสโครงการ : MRG5080287

ชื่อโครงการ: การประยุกต์ใช้วงจรกรองโวลเทอราสำหรับภาพจากอัลตราซาวน์แบบไม่เชิงเส้น

ชื่อนักวิจัย : ผู้ช่วยศาสตราจารย์ ดร. พรชัย พฤกษ์ภัทรานนต์

E-mail Address : pornchai.p@psu.ac.th

ระยะเวลาโครงการ : 2 ปี

บทคัดย่อ :

ปจจุบันมีการใช้ปรากฏการณ์ความไม่เป็นเชิงเส้นในการปรับปรุงคุณภาพของภาพจากอัล ตราซาวน์เพื่อให้การวินิจฉัยโรคทำได้ดียิ่งขึ้น การแยกสัญญาณไม่เชิงเส้นเป็นปัจจัยหลักในการ กำหนดคุณภาพของภาพที่ได้ โครงการวิจัยในรายงานฉบับนี้นำเสนอการประยุกต์ใช้วงจรกรองโวล เทอร์ราสำหรับภาพจากอัลตราซาวน์แบบไม่เชิงเส้น จุดประสงค์ของโครงการคือการวิเคราะห์ คุณสมบัติของวงจรกรองโวลเทอร์ราที่มีผลต่อคุณภาพของภาพจากอัลตราซาวนด์ทั้งในด้านความ คมชัดเชิงพื้นที่และด้านความคมชัดเชิงเปรียบต่าง แล้วหาวิธีการออกแบบวงจรกรองโวลเทอร์ราจาก คุณสมบัติที่ได้ศึกษาไว้ข้างต้น ผลการศึกษาที่สำคัญจากงานวิจัยนี้ คือได้วิธีการออกแบบวงจรกรอง ควอดราติกแบบใหม่ที่สามารถกำหนดรายละเอียดทางด้านเวลาและด้านความถื่อย่างเป็นอิสระต่อกัน ได้อย่างเหมาะสม ทำให้ได้วงจรกรองควอดราติกที่ให้คุณภาพของภาพจากอัลตราซาวนด์ที่ดีทั้งใน ด้านความคมชัดเชิงพื้นที่และด้านความคมชัดเชิงเปรียบต่าง ซึ่งเป็นความสามารถที่การประมวลผล แบบวงจรกรองเชิงเส้นไม่สามารถให้ได้ วิธีการออกแบบวงจรกรองควอดราติกแบบใหม่ได้รับการ ประเมินใช้กับข้อมูลภาพอัลตราซาวนด์ที่ได้จากการทดลองจริง ผลปรากฏว่าวิธีการออกแบบใหม่นี้ สามารถปรับปรุงคุณภาพของภาพจากอัลตราซาวนด์ให้ดีขึ้นทั้งในด้านความคมชัดเชิงพื้นที่และด้าน ความคมชัดเชิงเปรียบต่างอย่างมีนัยสำคัญ นอกจากนี้โครงการยังได้ทำการศึกษาการระบุเอกลักษณ์ ของระบบอัลตราซาวนด์ทางการแพทย์แบบไม่เชิงเส้นโดยใช้วงจรกรองโวลเทอร์ราลำดับที่สองเพื่อทำ การแยกองค์ประกอบสัญญาณไม่เชิงเส้น ผลการศึกษาพบว่าการระบุเอกลักษณ์โดยใช้วงจรกรองโวล เทอร์ราลำดับที่สองสามารถแยกองค์ประกอบสัญญาณไม่เชิงเส้นที่มีขนาดต่ำกว่าสัญญาณรบกวนได้ ซึ่งเป็นคุณสมบัติเฉพาะของเทคนิคที่การประมวลผลแบบวงจรกรองเชิงเส้นไม่สามารถให้ได้ ข้อดี ดังกล่าวเปิดโอกาสในการนำไปสู่การประยุกต์ใช้ปรับปรุงในทางวินิจฉัยด้านการแพทย์และการ วิเคราะห์คุณลักษณะของเนื้อเยื่อให้ดีขึ้นได้

คำหลัก: วงจรกรองโวลเทอร์รา ภาพจากอัลตราซาวน์แบบไม่เชิงเส้น ภาพจากอัลตราซาวน์ทาง การแพทย์

Abstract

Project Code: MRG5080287

Project Title: Applications of Volterra Filters for Nonlinear Ultrasound Imaging

Investigator: Assistant Professor Dr. Pornchai Phukpattaranont

E-mail Address: pornchai.p@psu.ac.th

Project Period: 2 years

Abstract:

Modern ultrasonic imaging modalities employ nonlinear phenomena to enhance diagnostic capabilities in medical applications. Nonlinear signal separation is a key factor in this success. Consequently, applications of Volterra filters for nonlinear ultrasound imaging are studied and results are presented in this report. The properties of Volterra filters that affect imaging qualities both in terms of contrast and spatial resolution are analyzed and used to formulate the design approach of Volterra filter for improving the quality of ultrasound images based on the investigated properties. The important finding is a novel design approach of a quadratic filter that allows for two degrees of freedom in optimizing time and frequency resolution independently. That is, axial resolution can be maintained while contrast resolution is maximized. Thus, it overcomes the trade-off in time frequency resolution problem appearing in linear bandpass filtering, which has only one degree of freedom in filter optimization. For example, in order to increase contrast resolution in linear bandpass filtering, the passband width of filter must be decreased. This unavoidably degrades axial resolution. Evaluation of the approach is demonstrated using a flow phantom target containing ultrasound contrast agent and a quality assurance ultrasound phantom consisting of resolution targets. Results show that the proposed method allows for obtaining the quadratic image with high contrast resolution and no apparent loss in axial resolution. In addition, a preliminary study of system identification based on Volterra filters applied in a nonlinear medical ultrasound system was carried out. The feasibility study shows that the system identification based on the second-order Volterra filter is capable of separating the second order nonlinearity embedded under the level of noise signal. This is a significant advantage of the method over a conventional linear filtering. Applications in practical use that the advantage of this new proposed method may allow for include medical diagnosis and tissue characterization.

Keywords: Volterra filter, Nonlinear ultrasound imaging, Medical ultrasound imaging

สรุปโครงการ (Executive summary)

1. ความสำคัญและที่มาของปัญหา (Importance and motivation of this research)

Conventional ultrasound techniques provide excellent clinical and diagnostic information about blood flow in arterial and venous macrovasculature of various systems. However, the sonographic detection of blood flow in small vessels of the microcirculation is a challenging problem. This is due to the fact that echoes from blood are much smaller than those from the surrounding tissue. Moreover, it is limited by other factors such as tissue motion (clutter), attenuation properties of the intervening tissue, and slow or low-volume flow. As a result, the echoes from blood are masked by those from surrounding tissue.

Recently, a significant improvement in blood flow detection by utilizing specific acoustic properties of ultrasound contrast agents (UCAs) has been achieved. That is, methods employing microbubbles provide enhancement in not only blood flow measurement of the backscattered Doppler signals but also gray-scale visualization of the flowing blood in the tissues of organs like the heart, liver, and kidney. Therefore, many reports of the improved diagnostic capabilities exploiting UCAs in clinical applications have been published in the past few years. Examples include improved discrimination between benign and malignant liver tumors [1], enhanced assessment of myocardial perfusion [2], and many others reported in [3]. This achievement exploits the nonlinear behavior from interaction between acoustic energy and UCAs to improve spatial and contrast resolution. Various modern imaging techniques rely on separating and enhancing nonlinear echoes including second harmonic (SH) and pulse inversion (PI) imaging.

In this proposal, we have investigated the use of a Volterra fillter model for separating the linear and nonlinear components of the beamformed radio frequency (RF) data in pulse-echo ultrasonic imaging in order to improve ultrasound image quality. Volterra filters have been extensively utilized as appropriate mathematical models for a wide variety of nonlinear physical phenomena. In particular, many important nonlinear effects from physical systems with mild nonlinearities can be estimated by the low-order Volterra filters (typically, either the 2nd or the 3rd order). Examples of numerous physics-related applications of truncated Volterra filters include elimination of nonlinear distortions in audio loudspeakers [4], equalization of nonlinear systems [5], and several other areas. The success of Volterra filters as nonlinear models for other physical systems provides the inspiration for applying them with nonlinear ultrasound problems.

2. วัตถประสงค์ (Objective of this research)

Each UCA imaging technique has its own limitation. SH imaging employs relatively narrowband pulses to improve separation between fundamental and harmonic components. Moreover, the selection of center frequency and duration of transmit pulse in imaging UCAs is a function of the UCA properties and transducer bandwidth characteristics. For example, in abdominal imaging, transmitting near the resonance frequency of the UCA, the loss in transmission efficiency may be compensated for by receive efficiency as the 2nd harmonic occurs closer to the center frequency of the imaging probe. Multi-pulse techniques such as

PI imaging have mitigated the need for transmitting narrowband pulses at the expense of reduction of the imaging frame rate.

To address some or all of limitations stated above, we have investigated the model-based approach, which employs the Volterra system to separate harmonic components of nonlinear echoes resulting from a single transmission covering the full (fundamental) bandwidth of the transducer. For simplicity and without loss of generality, we present post-beamforming nonlinear filter based on the second-order Volterra filter (SVF) to decompose UCA-backscattered signals into linear and quadratic components in this proposal. The specific objectives of this research are as follow:

- To analyze the SVF properties that affect imaging qualities both in terms of contrast and spatial resolution.
- To formulate the SVF design approach for improving contrast and spatial resolution of contrast-assisted ultrasonic imaging based on the investigated SVF properties.
- To survey other applications of Volterra filter to ultrasound medical problems, e.g. the study of nonlinear parameter B/A estimation based on the SVF model.

3. ระเบียบวิธีวิจัย (Research methodology)

Year 1

To understand SVF properties that affect imaging qualities both in terms of contrast and spatial resolution, we plan to investigate the SVF both in time and frequency domain. Recently, we have presented an insight of the quadratic filter for contrast-assisted ultrasonic imaging in the frequency domain [6]. It is shown that the understanding of quadratic kernel in the frequency domain allows for a new filter design approach. Also, we are motivated by the success of singular value decomposition (SVD) applying to two-dimensional FIR digital filters design as described in [7]. Consequently, we will further analyze the optimal quadratic filter in frequency domain using the SVD. After understanding the quadratic filter in frequency domain, we can directly design the optimal quadratic filter with no need of forming the system of linear equations and searching the optimal quadratic filter that provide the maximum contrast-to-tissue ratio. An obvious advantage of the direct design is the reduction in time and computational complexity. Additionally, the direct design may provide the optimal quadratic filter with less number of total coefficients. This is very desirable for real-time implementation of medical ultrasound imaging.

We also plan to investigate the characteristics of quadratic filter in time domain that affect imaging quality. It is shown in [8] that the quadratic kernel can be designed to be independent between time and frequency resolution with the constraints of non-zero only in the cross-diagonal. If this property is applicable in ultrasound nonlinear signal separation, the SVF can be used to overcome the trade-off between contrast and spatial resolution problem in ultrasound contrast agent imaging. That is, the quadratic filter will maximize contrast resolution without the sacrifice of spatial resolution. The property of independence between time and frequency resolution is going to be incorporated in our design approach to create the quadratic filter optimizing for both contrast and spatial resolution.

Year 2

We plan to evaluate the performance of quadratic filter from our design approach both in terms of contrast and spatial resolution. For the evaluation of spatial resolution, we will apply the quadratic filter to ultrasound data acquired from a quality assurance phantom. We also validate the quadratic filter from our proposed design with ultrasound RF data both *in vitro* (flow phantom) and *in vivo*. The quality of quadratic images will be reported.

Finally, we will survey the applications of the SVF to estimate acoustic nonlinearity parameter B/A. The acoustic nonlinearity parameter B/A is a measure of nonlinearity of a medium. It is shown to be a powerful parameter for characterizing tissue. For example, fatty soft tissues, which are more nonlinear than those without fat, also provide higher B/A values (approximately 10 compared with 7 [9]). In addition, the structure of biological media is shown to be dependent on ultrasonic nonlinearity parameter B/A [10]. We have demonstrated in [11] that nonlinearity parameter B/A can be estimated using the normalized input-output curve calculated from output signals of bandpass filter centered at the 2nd harmonic. However, if we determine nonlinearity parameter B/A using the normalized input-output curve calculated from output signals of the quadratic filter, we may obtain more accurate calculation of nonlinearity parameter B/A. This is due to the fact that the SVF is a model-based approach for detecting nonlinear signals. If we can precisely predict nonlinearity parameter B/A, we are able to distinguish media with different properties, e.g. not fatty and fatty soft tissues.

เอกสารอ้างอิง (References)

- [1] K. V. Ramnarine, K. Kyriakopoulou, P. Gordon, N. W. McDicken, C. S. McArdle, and E. Leen, "Improved characterization of focal liver tumors: dynamic power Doppler imaging using NC100100 echo-enhancer," *Eur. J. Ultrasound*, vol. 11, no. 2, pp. 95-104, May 2000.
- [2] C. Frischke, J. R. Lindner, K. Wei, N. C. Goodman, D. M. Skyba, and S. Kaul, "Myocardial perfusion imaging in the setting of coronary artery stenosis and acute myocardial infarction using venous injection of a second-generation echocardiographic contrast agent," *Circulation*, vol. 96, pp. 959-967, 1997.
- [3] D. Cosgrove, "Ultrasound contrast agents: An overview," Eur. J. Radiol., vol. 60, pp. 324-330, 2006.
- [4] M. Tsujikawa, T. Shiozaki, Y. Kajikawa, and Y. Nomura, "Identification and elimination of second-order nonlinear distortion of loudspeaker systems using volterra filter," in *Proc. IEEE ISCAS.*, 2000, vol. 5, pp. 249-252.
- [5] G. Lazzarin, S. Pupolin, and A. Sarti, "Nonlinearity compensation in digital radio systems," *IEEE Trans. commun.*, vol. 42, no. 2/3/4, pp. 988-998, Feb.-Apr., 1994.
- [6] P. Phukpattaranont and K. Chetpattananondh, "Post-Beamforming Second-order Volterra Filters for Contrast Agent Imaging: A Frequency-Domain Aspect," the 26th Symposium on Ultrasonic Electronics (USE-2005), Japan, Nov. 16-18, 2005, pp. 281-282.
- [7] W. H. Lu, H. P. Wang, and A. Antoniou, "Design of two-dimensional FIR digital filters by using the singular value decomposition," *IEEE Trans. Circuits Syst.*, vol. 37, no. 1, pp. 35-46, Jan. 1990.
- [8] J. Fang and L. E. Atlas, 'Quadratic detectors for energy estimation," *IEEE Trans. Signal processing*, vol. 43, no. 11, pp. 2582-2594, Nov. 1995.

- [9] R. L. Errabolu, C. M. Sehgal, R. C. Bahn, and J. F. Greenleaf, "Measurement of ultrasonic nonlinear parameter in excised fat tissues," *Ultrasound Med. Biol.*, vol. 14, no. 2, pp. 137–146, 1988.
- [10] J. Zhang, R. L. Magin, L. A. Frizzell, and F. Dunn, "Dependence of ultrasonic nonlinearity parameter B/A on cellular-level structure," in *Proc. IEEE Ultrason. Symp.*, 1988, pp. 975–978.
- [11] P. Phukpattaranont, "Determination of the Acoustic Nonlinearity Parameter B/A using Second Harmonic Signal Components," the 28th Thai Electrical Engineering Conference (EECON-28), Phuket, Thailand 2005, vol. 2, pp. 905-908.

4. แผนการดำเนินงานตลอดโครงการ (Research plan)

Activity			Month										
		1	2	3	4	5	6	7	8	9	10	11	12
Year 1 1. 2.	Investigate the properties of optimal quadratic filter both in time and frequency domain. Formulate a filter design approach	•				•		→					→
Year 2 1. 2.	Evaluate the approach using both <i>in-vitro</i> and <i>in-vivo</i> ultrasound data Study the estimation of a nonlinearity parameter B/A based on the SVF	•			•	•							-

5. ผลงาน

5.1 ผลงานตีพิมพ์ในวารสารวิชาการนานาชาติ (ระบุชื่อผู้แต่ง ชื่อเรื่อง ชื่อวารสาร ปี เล่มที่ เลขที่ และหน้า) หรือผลงานตามที่คาดไว้ในสัญญาโครงการ

มีจำนวน 2 เรื่อง ดังรายละเอียดต่อไปนี้

- P. Phukpattaranont and C. Limsakul, "Optimum quadratic filters for nonlinear ultrasonic imaging," Japanese Journal of Applied Physics, to be published in July 2009 [impact factor 1.309]
- P. Phukpattaranont, "Separation of nonlinear ultrasound signals based on second-Order Volterra system identification," *Japanese Journal of Applied Physics*, to be published in July 2009 [impact factor 1.309]

- 5.2 การนำผลงานวิจัยไปใช้ประโยชน์
 - เชิงพาณิชย์ (มีการนำไปผลิต/ขาย/ก่อให้เกิดรายได้ หรือมีการนำไปประยุกต์ใช้โดยภาคธุรกิจ/บุคคล ทั่วไป)
 - เชิงนโยบาย (มีการกำหนดนโยบายอิงงานวิจัย/เกิดมาตรการใหม่/เปลี่ยนแปลงระเบียบข้อบังคับหรือ วิธีทำงาน)
 - เชิงสาธารณะ (มีเครือข่ายความร่วมมือ/สร้างกระแสความสนใจในวงกว้าง)
 - เชิงวิชาการ (มีการพัฒนาการเรียนการสอน/สร้างนักวิจัยใหม่)
- 5.3 อื่นๆ (เช่น ผลงานตีพิมพ์ในวารสารวิชาการในประเทศ การเสนอผลงานในที่ประชุมวิชาการ หนังสือ การจดสิทธิบัตร)

การเสนอผลงานในที่ประชุมวิชาการ

- P. Phukpattaranont and C. Limsakul, "Optimum quadratic filters for nonlinear ultrasonic imaging," Proc. Symp. Ultrasonic Electronics (USE-2008), Nov. 11-13, 2008, pp. 283-284.
- P. Phukpattaranont, "Separation of nonlinear ultrasound signals based on second-Order Volterra system identification," *Proc. Symp. Ultrasonic Electronics (USE-2008)*, Nov. 11-13, 2008, pp. 343-344.
- P. Phukpattaranont and T. Nilmanee, "Nonlinear ultrasound system modeling based on the Volterra filter", in *Proc. ECTI International Conference (ECTI-CON 2008)*, May 15-16, 2008, vol. 1, pp. 553-556.
- P. Phukpattaranont, T. Nilmanee, C. Limsakul, and E. S. Ebbini, "Design of quadratic filters for contrast-assisted ultrasonic imaging," in *Proc. IEEE Ultrasonics Symposium*, Oct. 28-31, 2007, pp. 2211-2214
- T. Nilmanee and P. Phukpattaranont, "Quadratic filter for ultrasound contrast imaging," Proc. ThaiBME, December 18-19, 2007, vol. 1, pp. 42-47.

Table of Contents

Ta	able o	of Con	tents	i				
1	Introduction							
_	1.1		tance and Motivation	1 1				
	1.2	-	tives	2				
	1.3		ture Review	3				
	1.0	1.3.1	History and Development of Ultrasound Contrast Agent (UCA) .	3				
		1.3.2	Acoustic Properties of Microbubble Contrast Agent	5				
	1.4	Contra	ast Agent Imaging	9				
2	Sec	ond H	armonic Imaging	12				
	2.1	Introd	luction	12				
	2.2	Mater	ials and Methods	13				
		2.2.1	Experimental Setup and Data Acquisition	13				
		2.2.2	Power Spectrum	13				
		2.2.3	Linear Bandpass Filter (LBF)	14				
		2.2.4	Contrast Resolution	15				
	2.3							
		2.3.1	Frequency Characteristics	16				
		2.3.2	Stopband Attenuation	16				
		2.3.3	Fractional Bandwidth	19				
	2.4	Discus	ssion	19				
3	Qua	adratic	Filter Analysis	21				
	3.1	Introd	luction	21				
	3.2	Post-E	Beamforming Volterra Filter	21				
		3.2.1	Signal Separation Model	22				
		3.2.2	MNLS Estimation of SVF Coefficients	22				
		3.2.3	Regularization	24				
		3.2.4	Quadratic Images	25				
	3.3	Freque	ency Responses of Quadratic Filter	26				
	3.4	Result	ts	27				
		3.4.1	Image Enhancement	27				
		3.4.2	Frequency Responses	28				
	3.5	Discus	ssion	31				

4	Qua	dratic Filter Design and Evaluation	32				
	4.1	Introduction	32				
	4.2	Quadratic Filter Design	33				
	4.3	Materials and Methods	38				
	4.4	Results	39				
		4.4.1 Flow Phantom	39				
		4.4.2 Quality Assurance Phantom	42				
	4.5	Discussion	42				
5	Sec	ond-Order Volterra System Identification	47				
	5.1	Introduction	47				
	5.2	Theory	47				
		5.2.1 Nonlinear Pulse-Echo System	47				
		5.2.2 Volterra Filter	49				
		5.2.3 Identification of the SVF Model	50				
		5.2.4 Regularization	54				
	5.3	Materials and Methods	56				
		5.3.1 Details of the NPS					
		5.3.2 Identification Step	57				
		5.3.3 Validation Step	57				
	5.4	Results					
		5.4.1 Identification Results	57				
		5.4.2 Validation Results	61				
	5.5	Discussion	65				
6	Cor	Conclusions and Recommendations for Future Work					
	6.1	Conclusions					
	6.2	Recommendations for Future Study	67				
$\mathbf{B}^{\mathbf{i}}$	iblios	raphy	69				

Chapter 1

Introduction

1.1 Importance and Motivation

Conventional ultrasound techniques provide excellent clinical and diagnostic information about blood flow in arterial and venous macrovasculature of various systems. However, the sonographic detection of blood flow in small vessels of the microcirculation is a challenging problem. This is due to the fact that echoes from blood are much smaller than those from the surrounding tissue. Moreover, it is limited by other factors such as tissue motion (clutter), attenuation properties of the intervening tissue, and slow or low-volume flow. As a result, the echoes from blood are masked by those from surrounding tissue.

Recently, a significant improvement in blood flow detection by utilizing specific acoustic properties of ultrasound contrast agents (UCAs) has been achieved. That is, methods employing microbubbles provide enhancement in not only blood flow measurement of the backscattered Doppler signals but also gray-scale visualization of the flowing blood in the tissues of organs like the heart, liver, and kidney. Therefore, many reports of the improved diagnostic capabilities exploiting UCAs in clinical applications have been published in the past few years. Examples include improved discrimination between benign and malignant liver tumors [1], enhanced assessment of myocardial perfusion [2], and many others reported in [3]. This achievement exploits the nonlinear behavior from

interaction between acoustic energy and UCAs to improve spatial and contrast resolution. Various modern imaging techniques rely on separating and enhancing nonlinear echoes including second harmonic (SH) and pulse inversion (PI) imaging.

In this research, we have investigated the use of a Volterra fillter model for separating the linear and nonlinear components of the beamformed radio frequency (RF) data in pulse-echo ultrasonic imaging in order to improve ultrasound image quality. Volterra filters have been extensively utilized as appropriate mathematical models for a wide variety of nonlinear physical phenomena. In particular, many important nonlinear effects from physical systems with mild nonlinearities can be estimated by the low-order Volterra filters (typically, either the second or the third order) [4,5]. Examples of numerous physics-related applications of truncated Volterra filters include: (1) elimination of nonlinear distortions in audio loudspeakers [6], (2) algorithm for acoustic echo cancelation [7], (3) equalization of nonlinear systems [8], and several other areas. The success of Volterra filters as nonlinear models for other physical systems provides the inspiration for applying them with nonlinear ultrasound problems.

1.2 Objectives

Each UCA imaging technique has its own limitation. SH imaging employs relatively narrowband pulses to improve separation between fundamental and harmonic components. Moreover, the selection of center frequency and duration of transmit pulse in imaging UCAs is a function of the UCA properties and transducer bandwidth characteristics. For example, in abdominal imaging, transmitting near the resonance frequency of the UCA, the loss in transmission efficiency may be compensated for by receive efficiency as the second harmonic occurs closer to the center frequency of the imaging probe. Multi-pulse techniques such as PI imaging have mitigated the need for transmitting narrowband pulses at the expense of reduction of the imaging frame rate.

To address some or all of limitations stated above, we have investigated the

model-based approach, which employs the Volterra system to separate harmonic components of nonlinear echoes resulting from a single transmission covering the full (fundamental) bandwidth of the transducer. For simplicity and without loss of generality, we present post-beamforming nonlinear filter based on the second-order Volterra filter (SVF) to decompose UCA-backscattered signals into linear and quadratic components in this research. The specific objectives of this research are as follow:

- To analyze the SVF properties that affect imaging qualities both in terms of contrast and spatial resolution.
- To formulate the SVF design approach for improving contrast and spatial resolution of contrast-assisted ultrasonic imaging based on the investigated SVF properties.
- To survey other applications of Volterra filter to ultrasound medical problems, e.g. the study of nonlinear parameter B/A estimation based on the SVF model.

1.3 Literature Review

1.3.1 History and Development of Ultrasound Contrast Agent (UCA)

An ultrasound contrast agent (UCA) is an external substance that is usually introduced into the vascular system in order to enhance diagnostic and/or therapeutic capabilities in medical ultrasound, e.g. to improve the discrimination between normal and diseased tissue. Figure 1.1 shows one example of UCA, namely SonoVueTM (Bracco Research SA, Geneva, Switzerland) microbubbles, compared to red blood cells. Interest in UCA research originated from the observation of a cloud of echoes during the intracardiac injection of indocyanine green dye (a substance for measuring blood flow) by Gramiak and colleagues in 1968 while they performed M-mode echocardiography [9]. Afterward, it was discovered that those echoes were caused by microbubbles resulting from cavitation at the catheter tip [10,11]. Research on finding more appropriate substances to be used

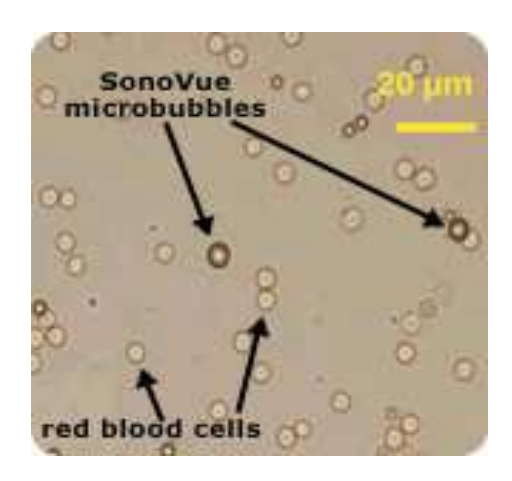


Figure 1.1: SonoVue microbubbles compared to red blood cells.

as contrast agents in ultrasound has been pursued since that time, but most vigorously in the last 10 years.

Ophir and Parker provided an excellent review of the state-of-the-art in the use of UCAs in ultrasound as of 1989 [12]. In this article, Ophir and Parker defined five categories of materials with different physical properties that may have potential to be used as UCAs. In particular, agents were based on free gas bubbles, encapsulated gas bubbles, colloidal suspensions, emulsions, and aqueous solutions. Appropriate contrast agents for ultrasound should be small and stable enough to circulate throughout the human body during a typical diagnostic examination. However, contrast agents at that time fell short on both criteria. Specifically, they could not reach the left heart after an intravenous injection because of the blocking from the capillary circulation in the lungs. This prevented the use of microbubbles as a contrast material in other organs such as the liver and kidney.

In order to extend the lifetime of microbubble contrast agents, many methods

have been investigated and several ways to stabilize microbubbles have been discovered. Currently, contrast agents that can survive the blood circulation of the lung are available [13,14]. The review by Frinking in 2000 reported that three transpulmonary UCAs were approved for clinical use. These are Levovist (Schering AG, Berlin, Germany), Albunex (Molecular Biosystems Inc., San Diago, USA), and Optison (Mallinckrodt, St. Louis, USA) [15]. In addition, more than 10 UCA from various manufacturers are under development and are being investigated for clinical use.

Most of current ultrasound contrast agents are based on encapsulated microbubbles. Compositions that allow them to traverse the lung capillary bed are the gaseous core with high molecular weights and the stabilized encapsulated shell. Gases with large molecules have low diffusion constants. As a result, their low diffusion rates reduce their dissolvability in fluids, such as blood and water [16]. On the other hand, the encapsulation with lipid or albumin shell prevents inner gases from the swift process of diffusing through the surrounding liquid.

1.3.2 Acoustic Properties of Microbubble Contrast Agent Scattering enhancement

Perfused tissues containing microbubble contrast agent provide higher echogenicity than that from normal tissues because of differences in acoustic properties of surrounding tissue media relative to those of microbubbles. In addition, this backscatter is possibly further increased by the oscillatory behaviors of microbubbles under acoustic pulse excitation. Consequently, conventional two-dimensional images of perfused organs can be produced with greater clarity. Details of physical mechanisms regarding backscatter enhancement resulting from microbubble contrast agents are given below.

Ultrasound is sensitive to particles with different acoustic properties (e.g., speed of propagation, density, and absorption) from the surrounding medium. The strength of backscattered signals from the mixed medium depends on its scattering cross-section (SCS) [17]. The SCS is defined as the scattered power from an incident plane wave

divided by the intensity of the incident wave. When the particle size is much smaller than the wavelength of insonating wavefront, the SCS can be expressed by (based on the Born approximation): [18]

$$SCS = \left[\frac{4}{9}\pi R^2 (kR)^4\right] \left\{ \left[\frac{\kappa_p - \kappa_m}{\kappa_m}\right]^2 + \frac{1}{3} \left[\frac{3\rho_p - 3\rho_m}{2\rho_p + \rho_m}\right]^2 \right\},\tag{1.1}$$

where $k = 2\pi/\lambda$ is the wavenumber, λ is the wavelength, R is the radius of the particle $\ll \lambda$, κ_p is the compressibility of the particle, κ_m is the compressibility of the medium, ρ_p is the density of the particle, and ρ_m is the density of the medium.

It can be seen from the formula in Equation 1.1 that a scattering strength is proportional to the fourth power of the ultrasound frequency and the sixth power of a particle radius. As a specific example, we calculate the SCS of a spherical air bubble with 1- μ m radius embedded in water under 3-MHz field using the following parameters: $\lambda = 5 \times 10^{-4}$ m, $k = 1.26 \times 10^{4}$ per m, $R = 1 \times 10^{-6}$ m, $\kappa_p = 7.65 \times 10^{-6}$ m²/N, $\kappa_m = 0.45 \times 10^{-9}$ m²/N, $\rho_p = 1.2$ kg/m³, and $\rho_m = 1000$ kg/m³. The resulting SCS of the bubble is 1×10^{-11} m². Note that the wavelength of ultrasound is much greater than the particle radius. In addition, the difference in compressibility $((\kappa_p - \kappa_m)/\kappa_m = 1.74 \times 10^4)$ significantly influences the SCS compared with the negligible term due to difference in density $((3\rho_p - 3\rho_m)/(2\rho_p + \rho_m) = 3)$.

For a comparison, the SCS of an iron sphere under the same conditions as the spherical air bubble case, except its compressibility ($\kappa_p = 5.5 \times 10^{-12} \text{ m}^2/\text{N}$) and density ($\rho_p = 7800 \text{ kg/m}^3$) values, is determined. The SCS of the iron particle is only $5 \times 10^{-20} \text{ m}^2$, which is 100 million times less than that from the bubble. This example demonstrates the substantial increase in SCS resulting from the gas-based particle. Similarly, microbubble contrast agents consisting of gaseous cores (e.g. free gas bubbles and encapsulated gas bubbles) are embedded in the blood pool, thus providing significant enhancement in backscattered signals.

When bubbles in a liquid are insonated with ultrasound, they also exhibit oscillatory motion resulting from their stiffness and inertia. While the stiffness of bubbles affects the oscillation of the enclosed gas core like spring, the inertia is caused by the mass of surrounding liquid. This bubble oscillation is important because it makes bubbles act as sound sources resulting in high SCS enhancement at a specific frequency, referred to as the resonant frequency. The resonance frequency of free gas bubbles can be approximated by [19]:

$$f_r = \frac{1}{2\pi R} \sqrt{\frac{3\gamma P_0}{\rho}},\tag{1.2}$$

where f_r is the resonance frequency, R is the radius of the bubble, P_0 is the pressure, γ is the ratio of specific heat, and ρ is the density of surrounding medium. The formula shows that the resonance frequency is inversely proportional to the bubble radius. Calculations of resonance frequencies of free gas bubbles in water using the following parameters: $P_0 = 1.01 \times 10^5$ Pa, $\gamma = 1.4$, and $\rho = 1000$ kg/m³, indicate that the bubbles with diameter values from 0.6 μ m to 6 μ m (typical diameters of contrast microbubbles available currently) provide their resonant frequencies in the frequency range of medical ultrasound (1-10 MHz).

Multiple Harmonic Generation

In addition to ultrasound frequency, bubble dynamics varies according to amplitudes of insonating pressure pulse. Characteristics of echoes from interactions between ultrasound and microbubbles can be divided into three categories according to levels of applied acoustic pressures. For the low amplitude pressure excitation, bubbles oscillation is linearly related to applied pressures, thus producing linear backscattered signals. As amplitudes of insonating pressure field increase, bubbles oscillate nonlinearly and produce harmonic echoes, i.e. the fundamental (f_0) and its higher multiple frequencies $(2f_0, 3f_0, ...)$ [20],[21]. These harmonic frequencies, especially the second harmonic, are significantly higher than those from the surrounding tissue and can be exploited in separating contrast echoes from the surrounding tissue medium.

For insonation at even higher pressures, the coating shells of microbubbles are

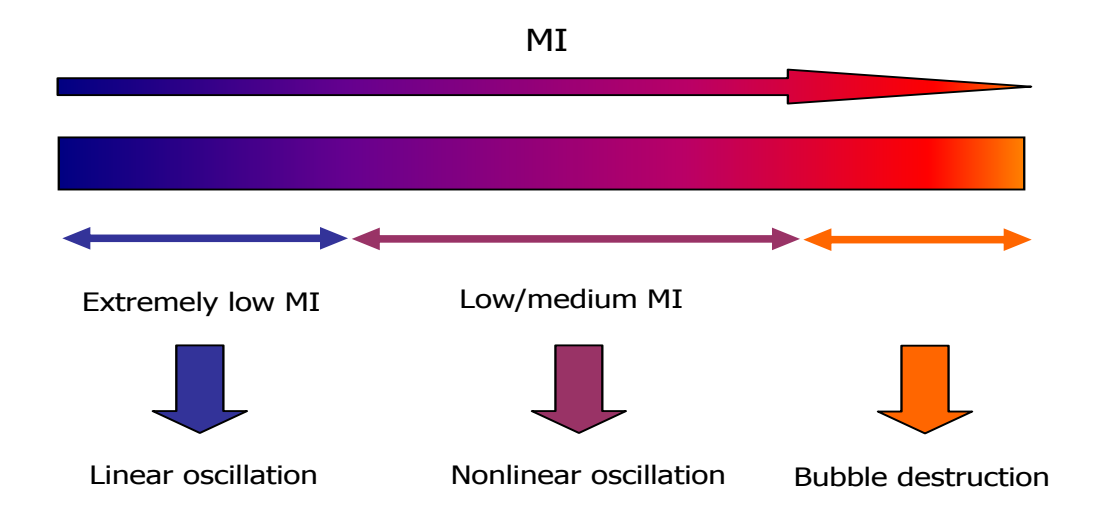


Figure 1.2: The responses of UCA bubble to ultrasound as a function of mechanical index.

disrupted and inner gases are dissolved in blood stream leading to suddenly high scattering and highly nonlinear echoes [22]. However, this irreversible process terminates the contrast effect because of bubble destruction. The level of bubble destruction is proportional to the mechanical index (MI), which is defined as [23,24]

$$MI = \frac{p_{-}}{\sqrt{f}},\tag{1.3}$$

where MI denotes the mechanical index, p_{-} is the peak negative pressure measured in MPa, and f is the transmit frequency measured in MHz. The higher the MI used in diagnostic ultrasound system, the higher possibility of bubble destruction. Imaging with low MI values to avoid bubble rupture is important for some imaging targets such as low blood flow organs. If bubbles are destroyed in those targets, low rates of contrast replenishment can interrupt continuous imaging diagnosis. On the other hand, replenishment curves are useful in forming parametric images reflecting function of organs. The responses of UCA microbubble to ultrasound as a function of mechanical index are summarized in Figure 1.2.

1.4 Contrast Agent Imaging

The early forms of UCA imaging relied on fundamental B-mode imaging. The rationale for this mode of image is based on Equation 1.1, i.e. increased SCS of microbubbles. This method only exploits enhanced strength of echoes due to high SCS of microbibbles in tissue media. However, in some imaging targets such as myocardium, the sensitivity of contrast agent detection is low due to the low microbubble population in perfused tissue. To enhance the detection sensitivity of microubble contrast agents, a number of imaging techniques based on other specific acoustic signatures of UCAs such as nonlinear and transient scattering have been developed. Some of these techniques that are currently used in pulse-echo medical ultrasound imaging as well as their strengths and weaknesses are given below.

In fundamental B-mode imaging, also known as standard B-mode imaging, UCAs increase the echogenicity from perfused tissues [12]. For example, in cardiac imaging, this results in improved endocardial border detection in left ventricular opacification, which leads to a better analysis of wall motion abnormalities [25]. Nevertheless, in the myocardium where the ratio of blood volume to tissue is low (approximately 10% [26]), the backscatter from the small number of microbubbles in vessels can be dominated by echoes from surrounding tissue. In this case, standard B-mode imaging offers inferior UCA detectability in the presence of tissue, stated as agent-to-tissue ratio [27].

Imaging techniques based on nonlinear oscillations have been designed for separating and enhancing nonlinear UCA echoes from a specified region of interest within the imaging field including second harmonic (SH) B-mode imaging and pulse inversion (PI) Doppler imaging [28]. SH imaging employs a fundamental frequency transmit pulse and produces images from the second harmonic component of received echoes by using a second harmonic bandpass filter (BPF) to remove the fundamental frequency. In order to increase UCA detection sensitivity in the limited transducer bandwidth condition, spectral overlap between fundamental and second harmonic parts need to be minimized

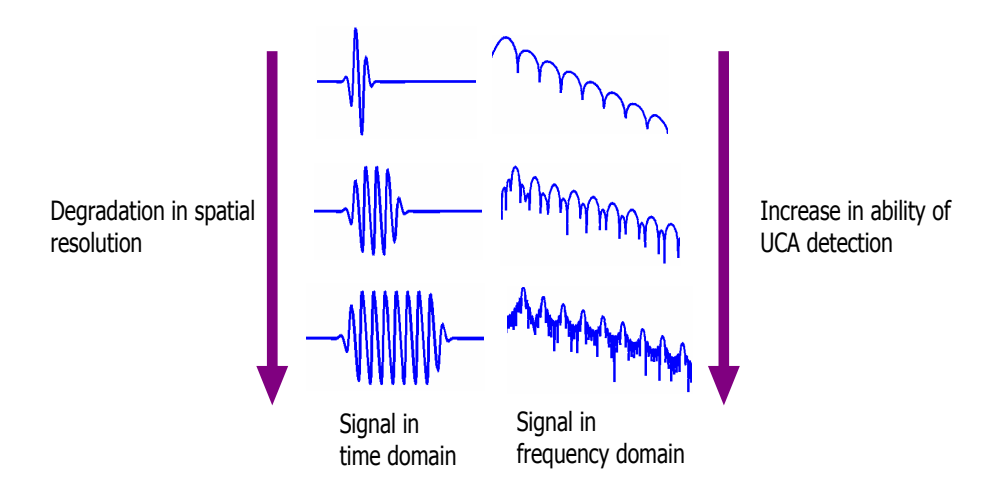


Figure 1.3: An inherent trade-off between contrast and spatial resolution in SH imaging.

by transmitting narrow-band pulses resulting in an inherent tradeoff between contrast and spatial resolution. The trade-off limitation of SH imaging is concluded and shown in Figure 1.3.

In PI imaging, a sequence of two inverted acoustic pulses with appropriate delay is transmitted into tissue. Images are produced by summing the corresponding two backscattered signals. In the absence of tissue motion, the resulting sum can be shown to contain only even harmonics of the nonlinear echoes [28]. PI imaging overcomes the tradeoff between contrast and spatial resolution because it utilizes the entire bandwidth of the backscattered signals [28]. As a result, superior spatial resolution can be achieved when compared with SH imaging. Moreover, it has been shown that PI imaging can be operated in a continuous imaging mode with low MIs [29]. PI imaging is sensitive to tissue motion because it is a multiple pulse technique; therefore, PI detection is combined with Doppler detection leading to a new technique called PI Doppler. The PI Doppler utilizes the advantages from both detection schemes and circumvents the tissue motion problem [28]. Nevertheless, an inherent multipulse technique of PI imaging results in the reduction of imaging frame rates. The principle of PI imaging is summarized and

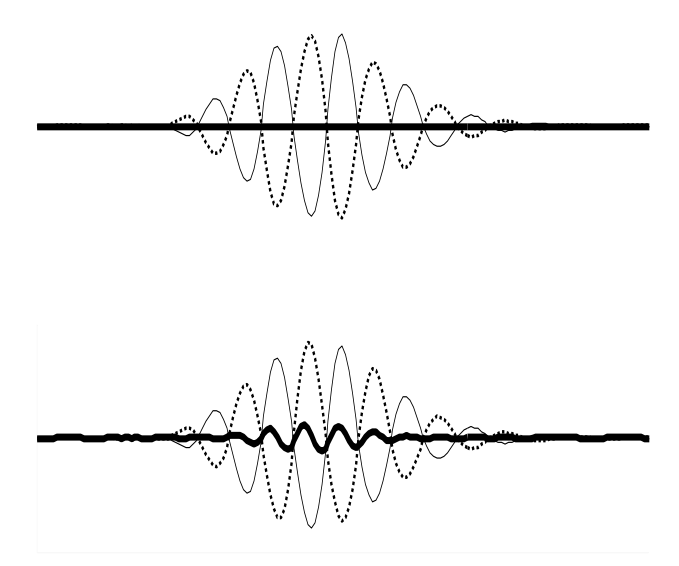


Figure 1.4: Harmonic separation using PI principle when the imaging target is stationary. Top: A linear positive pulse (Thin line) plus a linear negative pulse (Dotted line) is zeros (Thick line). Bottom: A nonlinear positive pulse (Thin line) plus a nonlinear negative pulse (Dotted line) is the remaining even harmonic components (Thick line).

shown in Figure 1.4.

In addition, when ultrasound propagates in media, it slightly exhibits higher harmonic frequencies $(2f_0, 3f_0, ...)$ because the compressional cycle of the sound wave moves slightly faster than the rarefactional cycle does and the sound wave becomes distorted. Although nonlinear propagation can be used to improve image quality in tissue harmonic imaging (THI) [23], it reduces the sensitivity to separate UCA echoes from tissue echoes not only in SH and PI imaging but also in other imaging techniques that employ nonlinearity from contrast agents.

Chapter 2

Second Harmonic Imaging

2.1 Introduction

This chapter describes the second harmonic frequency characteristic and second harmonic image generation from pulse-echo signals of UCA. Based on the differences in frequency of ultrasound data from two different media, ultrasound signals are classified into two classes, i.e., UCA and tissue. We show the frequency characteristic of the UCA signals from an *in vivo* target to demonstrate this nonlinear behavior. Then, the difference in frequency components of the UCA and tissue data is used as a reference to design a linear bandpass filter (LBF) in order to separate the UCA signals from tissue echoes. The LBF is designed using the Parks-McClellan algorithm. We find that the appropriate fractional bandwidth (FB) and stopband attenuation of the LBF are 15% - 25% and 40 - 50 dB, respectively. The imaging quality for medical ultrasound purposes, by utilizing the information from the frequency contents of contrast-assisted ultrasound data, has been improved. Results show that the images produced from the output signals of the optimal LBF are superior to the original B-mode images both in terms of contrast and spatial resolution.

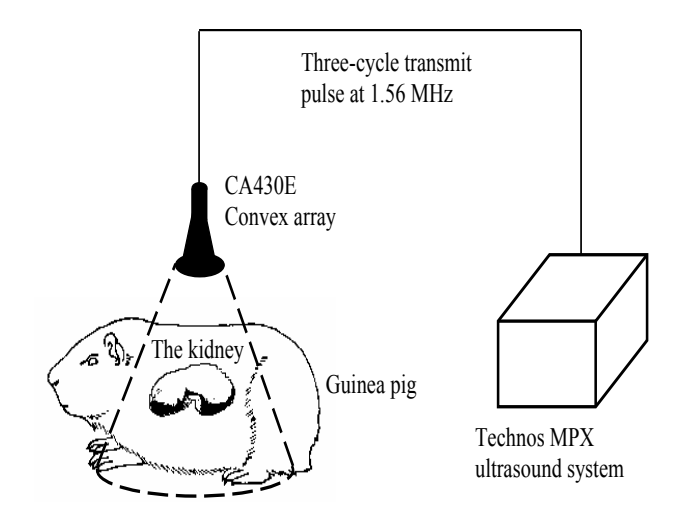


Figure 2.1: The imaging setup for the guinea pig's kidney.

2.2 Materials and Methods

2.2.1 Experimental Setup and Data Acquisition

The experiment was conducted in vivo on a guinea pig. Bolus injections of SonoVueTM (Bracco Research SA, Geneva, Switzerland), a UCA consisting of sulphur hexafluoride gas bubbles coated by a flexible phospholipidic shell, were administered with a concentration of 0.01 mL/kg. Figure 2.1 shows the imaging setup for the guinea pig's kidney. Three-cycle pulses at 1.56 MHz were transmitted with a mechanical of index 0.158 to scan the kidney of the guinea pig. Radio frequency (RF) data were acquired with 16-bit resolution at 20-MHz sampling frequency. In addition, all RF data were recorded and saved for off-line processing by the Technos MPX ultrasound system (ESAOTE S.p.A, Genoa, Italy) with a convex array probe (CA430E; ESAOTE S.p.A, Genoa, Italy).

2.2.2 Power Spectrum

After data acquisitions, we determined the power spectrum of RF A-lines from the UCA regions compared with those from the tissue regions. Power spectrum of A-line data was obtained using the periodogram method with a weighted sequence. The multiplication of the weighted sequence, i.e. window, in the time domain is convolution in the frequency

domain, so some resolution gets lost by smearing and spectral leakage. However, the trend of the signal's estimated power spectral density (PSD) can be enhanced by the use of a window function with faster decaying side-lobes. The expression used to calculate the power spectrum is given by

$$S\left(e^{j\omega}\right) = \frac{\frac{1}{n} \left|\sum_{i=1}^{n} w_i x_i^{-j\omega i}\right|^2}{\frac{1}{n} \sum_{i=1}^{n} \left|w_i\right|^2},\tag{2.1}$$

where $S(e^{j\omega})$ is a power spectrum, $[x_1, \ldots, x_n]$ is a signal sequence, and $[w_1, \ldots, w_n]$ is a weighted sequence. This expression is an estimate of the power spectrum of the signal sequence $[x_1, \ldots, x_n]$ weighted by the window sequence $[w_1, \ldots, w_n]$. A periodogram uses an n-point FFT to compute the PSD as $S(e^{j\omega})/F$ where F is a sampling frequency. Twenty-one segments of A-lines from the UCA and tissue regions were used to determine power spectra. Each segment consisted of 201 samples of data. A Hanning window was chosen as the weighted signal sequence in this paper. An n-point symmetric Hanning window can be expressed as

$$w[k+1] = 0.5 \left(1 - \cos\left(2\pi \frac{k}{n+1}\right)\right), k = 0, \dots, n-1.$$
 (2.2)

2.2.3 Linear Bandpass Filter (LBF)

In this work, we use the Parks-McClellan algorithm (Parks and McClellan, 1972) to design a linear bandpass filter (LBF). The designed filters exhibit an equiripple behavior in their frequency response, and hence are also known as equiripple filters. The parameters for the LBF design, i.e. fractional bandwidth and stopband attenuation, are chosen to maximize the difference in the spectra of echo signals from the UCA and tissue regions. The LBF with optimal parameters should enhance the UCA components but suppress the tissue signals. Parameters to be considered for the design of the LBF are shown in Figure 2.2. The fractional bandwidth of the LBF can be obtained by

$$FB = \frac{2f_B}{f_C} \times 100\%,$$
 (2.3)

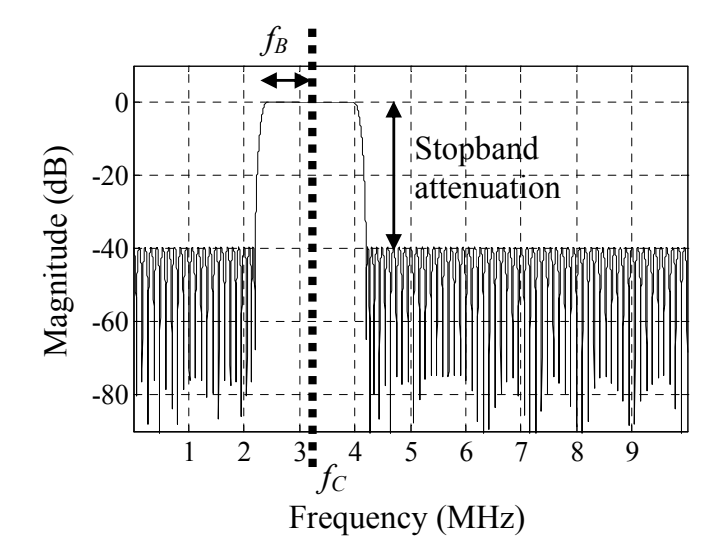


Figure 2.2: Two parameters considered in the design of an optimal LBF: Fractional bandwidth (FB) and stopband attenuation.

where FB is a fractional bandwidth, f_B is one-half of a defined passband in the filter specification, and f_C is a center frequency. In addition, stopband attenuation is defined in terms of dB below the passband of the filter. Signal outputs from the optimal LBF are used to make a gray-level image, which provides better quality for medical diagnosis.

2.2.4 Contrast Resolution

We measured the contrast resolution of images using a contrast-to-tissue ratio (CTR), which is given by

$$CTR = 10 \log \frac{\bar{P}_C}{\bar{P}_T},\tag{2.4}$$

where \bar{P}_C and \bar{P}_T are the average power of signals in the UCA and tissue regions, respectively. The average power is obtained by

$$\bar{P} = \frac{1}{IJ} \sum_{i=1}^{I} \sum_{j=1}^{J} x_{ij}^{2}, \tag{2.5}$$

where x_{ij} is the signal in the reference region. We use CTR as a measurement of the LBF's capability in extracting second harmonic components. The appropriate LBF for

producing a gray-level image with enhanced quality should provide a high CTR value.

2.3 Results

2.3.1 Frequency Characteristics

The gray image of the guinea pig's kidney is shown in Figure 2.3(a) with a 50 dB dynamic range. The reference tissue and UCA regions used for calculation of the power spectra are on the left and right white boxes, respectively. Each region consists of 21 A-line pulse-echo signals. To investigate more details of the frequency characteristic of pulse-echo signals, we show the average spectra and standard deviation (SD) of 21 A-lines from the tissue and UCA regions in Figure 2.3(b) and (c), respectively. We can see that every A-line signal from the UCA region exhibits the second harmonic frequency. On the contrary, the A-line signal from the tissue region contains only the fundamental frequency. Average spectra determined from 21 A-line signals of the tissue and UCA regions on the left and right boxes of Figure 2.3(a) are shown in Figure 2.3(d) using dotted and solid lines, respectively. We can see that the harmonic spectrum of the UCA echoes (solid line) between 2.5 and 4 MHz band are broader than those from tissue echoes (dotted line). This result obviously shows the fundamental and second harmonic frequency generation due to the UCAs. On the other hand, the signals from the tissue regions contain only the transmitted fundamental frequency.

2.3.2 Stopband Attenuation

We can clearly see in Figure 2.3(d) that the UCA components are higher than the tissue components in the frequency range between 2.5 and 4 MHz. Based on this observation, the center frequency is selected to be 3.2 MHz for all designs of the LBF in this paper. In order to investigate the appropriate stopband attenuation, we designed the LBF with a fixed FB of 12.5%. The gray-level images of the guinea pig's kidney resulting from various stopband attenuations with fixed fractional bandwidth at 12.5% are shown in Figure 2.4. Images after filtering with the LBF produced from the stopband attenuation

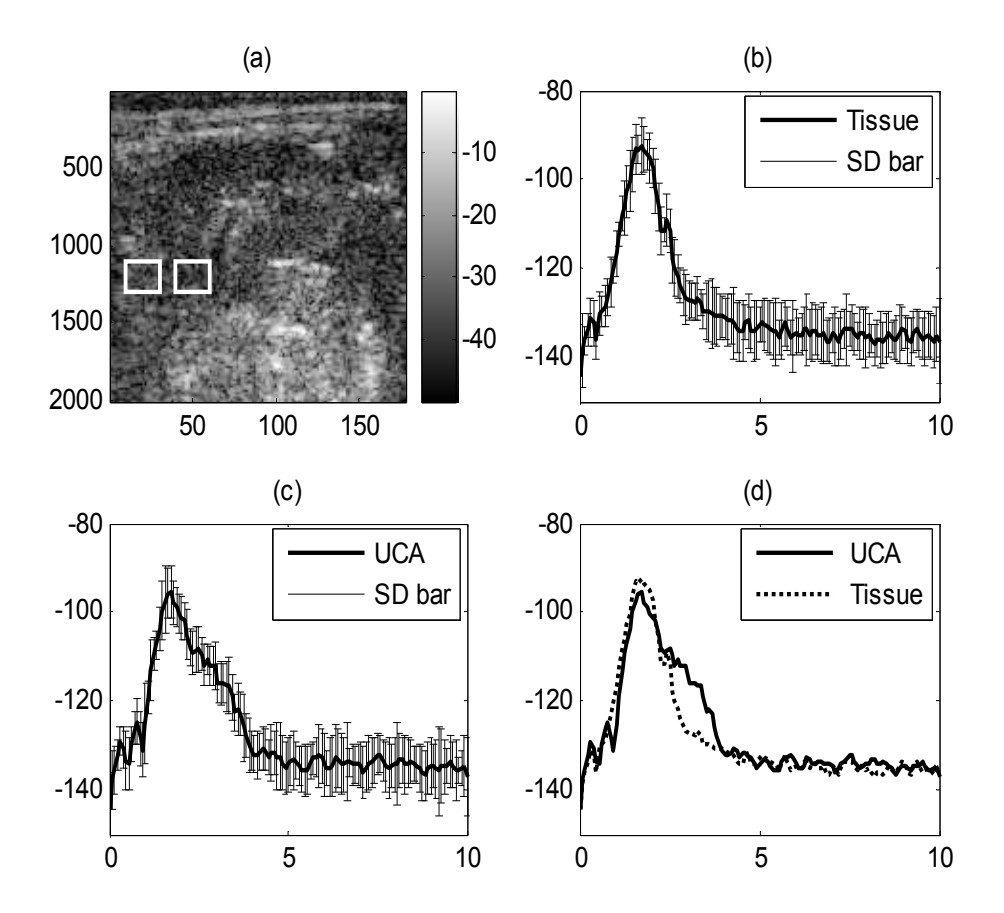


Figure 2.3: (a) B-mode image of the guinea pig's kidney (b) Average spectra and standard deviation (SD) of 21 A-line signals from the tissue region. (c) Average spectra and SD of 21 A-line signals from the UCA region. (d) Average spectra of tissue and UCA signals from the left and right boxes of (a).

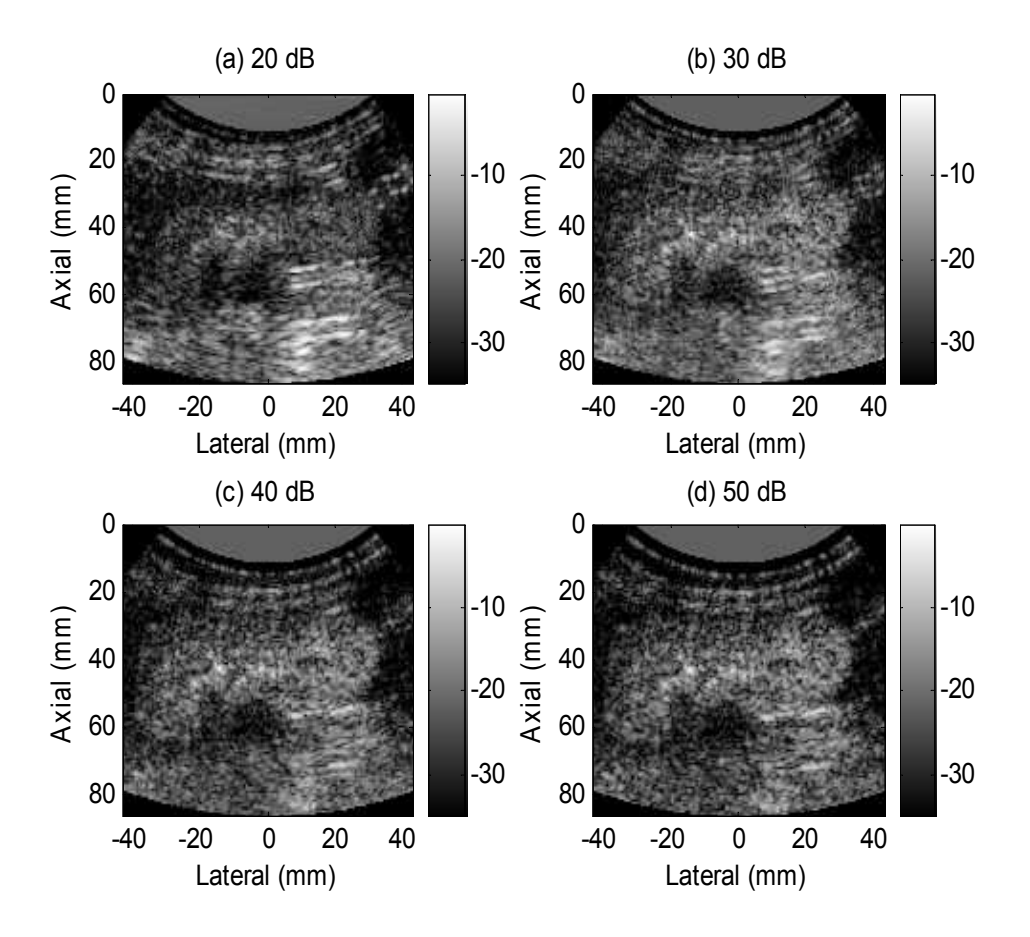


Figure 2.4: Gray-level images of the guinea pig's kidney from signals after filtering with the LBF by varying stopband attenuation to be 20, 30, 40, and 50 dB. FB is fixed at 12.5%. The CTR values from the images in (a), (b), (c), and (d) are 2.0, 8.5, 11.8, and 12.7 dB, respectively.

of 20, 30, 40, and 50 dB are shown in Figure 2.4(a), (b), (c), and (d), respectively. It is shown that images in Figure 2.4(c) and (d) have a comparable contrast resolution and are better than those from images in Figure 2.4(a) and (b). We can clearly visualize the kidney shape and large vascular structures inside the kidney. In addition, CTR values from images in Figure 2.4(a), (b), (c), and (d) are 2.0, 8.5, 11.8, and 12.7 dB, respectively. These are in agreement with the visualized inspection.

2.3.3 Fractional Bandwidth

Figure 2.5 shows gray-level images from the LBF with a different fractional bandwidth at the fixed stopband attenuation of 40 dB. Images after filtering with the LBF produced from the FB of 10, 15, 25, and 50% are shown in Figure 2.5(a), (b), (c), and (d), respectively. It can be seen that the LBF with FB from 10% to 25% are appropriate for enhancing imaging quality in terms of contrast resolution. However, spatial resolution is improved when the FB of the LBF increases. In other words, the LBF with FB 25% provides the best image in terms of spatial resolution. The CTR values of images in Figure 2.5(a), (b), (c), and (d) are 11.2, 11.4, 11.0, and 2.8 dB, respectively. They agree well with the visualization.

2.4 Discussion

We demonstrated the nonlinear properties from the interaction between the UCA and transmitted acoustic energy. The second harmonic frequency of pulse-echo signals from the UCA region is significantly higher than those from the surrounding tissue region. The imaging quality of medical ultrasound images can be enhanced by employing these second harmonic components. Gray-level images produced using the LBF with optimal fractional bandwidth (15 - 25%) and stopband attenuation (40 - 50 dB) are better than the original B-mode images both in terms of contrast and spatial resolution. We also explored the effects of filter ripples. It turns out that passband ripples have very slight effects to the imaging quality. However, the lower passband ripple results in the higher filter length. This leads to more computational complexity. Consequently, the passband ripple of approximately 0.5 dB is suggested for contrast-assisted ultrasonic imaging. Results of ultrasound image improvement produced from linear bandpass filtering are used as a baseline for comparison with those from the novel proposed nonlinear filtering based on Volterra model.

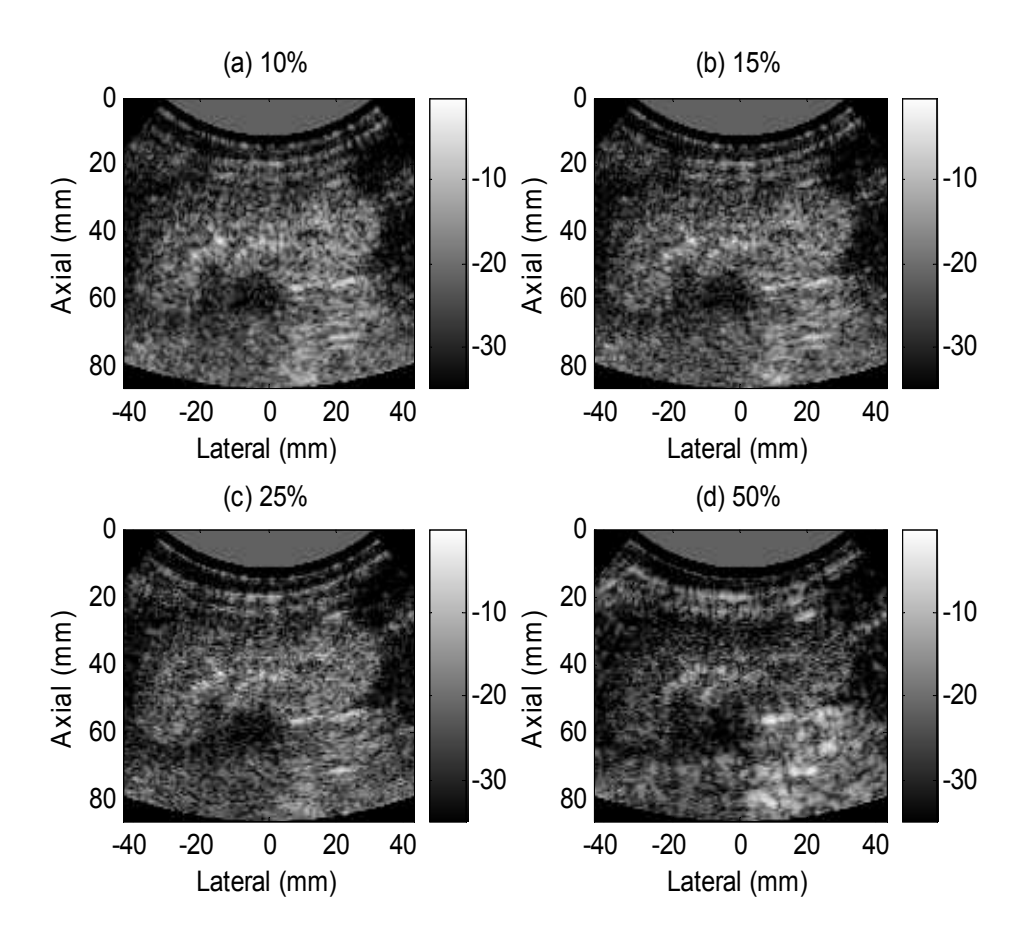


Figure 2.5: Gray-level images of the guinea pig's kidney from signals after filtering with the LBF by varying FB to be 10, 15, 25, and 50%. Stopband attenuation is fixed at 40 dB. The CTR values of the images in (a), (b), (c), and (d) are 11.2, 11.4, 11.0, and 2.8 dB, respectively.

Chapter 3

Quadratic Filter Analysis

3.1 Introduction

In this chapter, we present the design approach for quadratic filter (QF) from postbeamforming Volterra filter. Imaging results demonstrate that quadratic B-mode (QBmode) images produced from the output signal of optimum QF provide high contrast of UCA over surrounding tissue regions. In addition, we describe the second-order frequency response (SFR), i.e. $H_2(e^{j\omega_1}, e^{j\omega_2})$, of the quadratic filter and its contribution to the spectra of quadratic signal output. This tool allows for not only understanding the contrast enhancement mechanisms of QB-mode images but also opening the opportunity for novel QF design resulting in images with better quality for medical diagnosis.

3.2 Post-Beamforming Volterra Filter

We have demonstrated the validity of a second order Volterra system as a model for pulse-echo ultrasonic imaging data from tissue mimicking media in [30]. An input-output system identification approach was used to estimate the coefficients of the linear and quadratic components of the SVF in the frequency domain. However, while the system identification study was necessary to establish the applicability of SVF to ultrasound pulse-echo data, it is not useful for imaging purposes as it requires access to both the input and the echo data from distinct scatterers in the tissue-mimicking media. An appropriate approach for imaging operates on the beamformed RF data to separate the

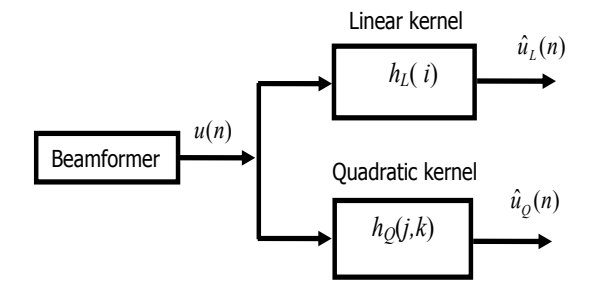


Figure 3.1: Separation of beamformed RF data into linear and quadratic components using the SVF.

linear and quadratic components regardless of the input. This signal separation approach allows us to extract the linear and quadratic signal components from the beamformed data to form linear and/or quadratic images separately or compounded.

3.2.1 Signal Separation Model

Figure 3.1 shows a simple block diagram of the imaging system based on the SVF. The SVF operates on the beamformer output to produce the linear and quadratic components, $\hat{u}_L(n)$ and $\hat{u}_Q(n)$, respectively. Estimates of the total beamformer output can be obtained from these components simply by adding them

$$\hat{u}(n) = \hat{u}_L(n) + \hat{u}_Q(n),$$
(3.1)

where $\hat{u}(n), \hat{u}_L(n)$, and $\hat{u}_Q(n)$ are the total, linear and quadratic estimations, respectively. The separation of the linear and quadratic components can be achieved once the coefficients of the kernels, $h_L(i)$ (linear) and $h_Q(j,k)$ (quadratic) are found. In the following subsection, we describe a minimum-norm least-squares (MNLS) approach for determining these coefficients.

3.2.2 MNLS Estimation of SVF Coefficients

Assume the RF echo signal, u(n), is composed of linear and quadratic components, i.e. $u(n) = u_L(n) + u_Q(n)$. The quadratic component may result from nonlinear propagation

in tissue and/or nonlinear oscillations of UCA in response to transmit imaging pulse. The response of a quadratically nonlinear system with memory can be predicted by a (discrete) second-order Volterra model operating on the m past samples as follows:

$$\hat{u}(n+1) = \sum_{i=0}^{m-1} u(n-i)h_L(i)
+ \sum_{j=0}^{m-1} \sum_{k=j}^{m-1} u(n-j)u(n-k)h_Q(j,k),$$
(3.2)

where $h_L(i)$ and $h_Q(j, k)$ are the linear and quadratic filter coefficients, respectively. Note that while $\hat{u}(n+1)$ is nonlinear with respect to the beamformed data, it is linear with respect to the coefficients of the linear and quadratic kernels of the SVF. Recognizing this fact, one can rewrite Equation 3.2 in vector form:

$$\hat{u}(n+1) = \mathbf{u}^{T}(n)\mathbf{h},\tag{3.3}$$

where the data vector, $\mathbf{u}(n)$, is defined at sample n as

$$\mathbf{u}(n) = [u(n), u(n-1), u(n-2), \dots, u(n-m+1),$$

$$u^{2}(n), u(n)u(n-1), \dots, u^{2}(n-m+1)]^{T},$$

and the filter coefficient vector, h, can be expressed as

$$\mathbf{h} = [h_L(0), h_L(1), h_L(2), \dots, h_L(m-1), h_Q(0,0), h_Q(0,1), \dots, h_Q(m-1, m-1)]^T,$$

where m is the system order and superscript T denotes the transpose. The total number of independent filter coefficients, N, is equal to $(m^2 + 3m)/2$ assuming a symmetrical quadratic kernel (i.e., $h_Q(j,k) = h_Q(k,j)$). Similarly, $\hat{u}(n+2), \hat{u}(n+3), ..., \hat{u}(n+M)$ can be represented in the form of Equation 3.3 and expressed in the matrix form

$$\mathbf{f} = \mathbf{Gh},\tag{3.4}$$

where the vector \mathbf{f} and the data matrix \mathbf{G} are defined as

$$\mathbf{f} = [u(n+1), u(n+2), \dots, u(n+M)]^T$$

and

$$\mathbf{G} = [\mathbf{u}(n), \mathbf{u}(n+1), \dots, \mathbf{u}(n+M-1)]^T,$$

where M is the number of linear equations (observations). The MNLS solution can be derived using the SVD of \mathbf{G} , which is defined as

$$\mathbf{G} = \mathbf{U} \mathbf{\Sigma} \mathbf{V}^T = \sum_{i=1}^r \sigma_i \mathbf{u}_i \mathbf{v}_i^T, \tag{3.5}$$

where Σ is a $M \times N$ diagonal matrix with singular values $\sigma_1 \geq \sigma_2 \geq \ldots \geq \sigma_r > \sigma_{r+1} = \ldots = \sigma_p = 0$ $(p = \min\{M, N\})$ and $r \leq \min\{M, N\}$ is the rank of \mathbf{G} . The matrices $\mathbf{U}(M \times M)$ and $\mathbf{V}(N \times N)$ are formed from the columns $\{\mathbf{u}_i\}_{i=1}^M$ and $\{\mathbf{v}_i\}_{i=1}^N$, which are the orthogonal eigenvectors of $\mathbf{G}\mathbf{G}^T$ and $\mathbf{G}^T\mathbf{G}$, respectively [31]. The MNLS solution is then given by

$$\mathbf{h}_{\text{MNLS}} = \sum_{i=1}^{r} \frac{\mathbf{u}_{i}^{T} \mathbf{f}}{\sigma_{i}} \mathbf{v}_{i}. \tag{3.6}$$

3.2.3 Regularization

The SVD of **G** forms a basis for regularization by appropriate selection of singular modes that enhance the contrast between UCA and tissue regions in the image. A solution based on the constrained optimization problem, which is the general form of the regularization, can be expressed as

$$\mathbf{h}_{\text{Reg}} = \sum_{i=1}^{r} \frac{\sigma_i}{\sigma_i^2 + \gamma_i R_i^2} \mathbf{u}_i^T \mathbf{f} \mathbf{v}_i, \tag{3.7}$$

where γ_i is an appropriately chosen threshold for the *i*th singular mode and R_i^2 is quadratic ratio resulting from the quadratic kernel obtained from the *i*th singular mode.

The TSVD regularization, also known as rank reduction regularization [32], used in our previous work can be derived from Equation 3.7. When γ_i is chosen to be

$$\gamma_i = \begin{cases} 0 & : & i \le k \\ \infty & : & k < i \le r \end{cases} , \tag{3.8}$$

where $k \leq r$ is the number of singular modes used to compute the estimate, the kth order TSVD solution is given by

$$\mathbf{h}_{\text{TSVD}}(k) = \sum_{i=1}^{k} \frac{\mathbf{u}_i^T \mathbf{f}}{\sigma_i} \mathbf{v}_i. \tag{3.9}$$

In the context of the linear and quadratic prediction approach, the estimation error (i.e., the root mean square value of the residual between observable and predicted data) decreases monotonically with k. A criterion for choosing an appropriate value of k is needed. In the context of contrast-agent imaging, an obvious criterion is the contrast-to-tissue ratio (CTR)

$$CTR = 10 \log_{10} \left(\frac{\overline{P}_C}{\overline{P}_T} \right), \tag{3.10}$$

where \overline{P}_C is the average power of signals in a UCA region and \overline{P}_T is the average power of signals in a tissue region. The average power of signals in a given region, \overline{P} , can be expressed as:

$$\overline{P} = \frac{1}{IJ} \left(\sum_{i=1}^{I} \sum_{j=1}^{J} x_{ij}^2 \right),$$
 (3.11)

where x_{ij} is the signal in that region. The CTR provides a measure of performance reflecting the agent-to-tissue specificity in the context of UCA imaging.

3.2.4 Quadratic Images

Quadratic images are obtained from quadratic components of the second-order Volterra model. The coefficients of the SVF are derived from the beamformed RF data taken from a representative region on a standard B-mode image. Details of the algorithm to produce the quadratic image are as follows.

From the standard B-mode image, a UCA region and a tissue region are defined for the CTR computation. In general, we try to find regions at the same depth and with the same beam angle with respect to the axis of the imaging array. Furthermore, whenever possible, we chose multiple overlapping subregions to obtain multiple CTR values at different depths. Once the CTR reference regions are defined, a segment of RF data from an axial line is selected to form a system of linear equations according to Equation 3.2. This segment can be selected from the tissue or the UCA region as long as the appropriate regularization of the MNLS solution is sought. For example, when TSVD is used for regularization, CTRs of quadratic signals calculated from various orders of

TSVD solutions are collected. With a defined range of system orders, a CTR plane as a function of truncation parameters and system orders is determined. Filter coefficients for the quadratic imaging generation are obtained from a truncation parameter and a system order that give the highest CTR value in the CTR plane. Of course, the TSVD approach can be used to obtain the coefficients of the quadratic kernel, , for a predetermined filter order . This may be necessary from the implementation point of view, when the size of the kernel is to be kept at manageable level. The results are obtained with low-order filter to emphasize the practicality of the Volterra filter approach.

The quadratic image is produced by applying the quadratic filter coefficients to the beamformed RF data throughout the standard B-mode image to estimate the quadratic component

$$\hat{u}_Q(n+1) = \sum_{j=0}^{m-1} \sum_{k=j}^{m-1} u(n-j)u(n-k)\hat{h}_Q(j,k), \qquad (3.12)$$

where $\hat{h}_Q(j,k)$ is the estimated quadratic kernel.

3.3 Frequency Responses of Quadratic Filter

As described in last section, the QB-mode image is produced using a quadratic filter, in which the relation between input x(n) and output y(n) can be expressed as

$$y(n) = \sum_{k_1=0}^{N-1} \sum_{k_2=0}^{N-1} h_2(k_1, k_2) x(n - k_1) x(n - k_2),$$
(3.13)

where $h_2(\cdot,\cdot)$ represents the quadratic kernel and N is the system memory. The quadratic kernel for contrast agent imaging is obtained by forming a system of linear equations from a segment of beamformed RF data and solving for filter coefficients to minimize the error from the linear plus quadratic predictor (For complete details of the algorithm, please see [33]). The QB-mode image is produced by applying the optimal kernel to the beamformed RF data throughout the B-mode image.

In this section, we analyze the characteristics of the optimal quadratic filter, which is capable of enhancing UCA over tissue, in the frequency domain. The inputoutput relation of the quadratic filter shown in Equation 3.13 in the frequency domain is given by

$$Y(e^{j\omega}) = \frac{1}{2\pi} \int_0^{2\pi} \int_0^{2\pi} H_2(e^{j\omega_1}, e^{j\omega_2}) X(e^{j\omega_1}) X(e^{j\omega_2}) d\omega_1 d\omega_2$$
 (3.14)

under the assumption

$$\omega_1 + \omega_2 = \omega, \tag{3.15}$$

where $Y(e^{j\omega})$ is the discrete-time Fourier transform (DTFT) of y(n), $X(e^{j\omega})$ is the DTFT of x(n), and $H_2(e^{j\omega_1}, e^{j\omega_2})$ is the 2D DTFT of $h_2(\cdot, \cdot)$. Note that the observed quadratic signal component at ω is the result of the sum of mixing all frequency components ω_1 and ω_2 such that $\omega_1 + \omega_2 = \omega$ weighted by the quadratic frequency response at $\omega_1 + \omega_2 = \omega$.

3.4 Results

3.4.1 Image Enhancement

We use the RF data acquired in vivo to investigate characteristics of the optimal quadratic filter in the frequency domain (Please see [33] for details of the experimental setup and quadratic filter derivation). Figure 3.2(a) shows the B-mode image of the kidney after the injection of 0.01 mL/kg UCAs acquired using 3-cycle 1.56-MHz pulse (MI = 0.158) transmissions. Average spectra of tissue and UCA signals in the left and right boxes of Figure 3.2(a) are shown in Figure 3.2(b). We can clearly see that harmonic spectra of UCA echoes (solid) between 2 MHz and 4 MHz frequency band are broader than those from tissue echoes (dotted line). Figure 3.2(c) shows the optimal quadratic filter used to produce QB-mode images. The filter is a square matrix with size 57 by 57. The resulting QB-mode image processed with the quadratic filter shown in Figure 3.2(c) is shown in Figure 3.2(d). One can clearly see the improvement of image quality.

This significant enhancement of QB-mode image can be explained using the relation described in Equation 3.14.

3.4.2 Frequency Responses

Figure 3.3 shows a filled contour plot of magnitude of frequency responses in the (ω_1, ω_2) plane. The filled contour plot displays isolines calculated from the magnitude of frequency function in the (ω_1, ω_2) plane and fills the areas between the isolines using constant colors. The magnitude frequency responses obtained using RF data in the tissue $(|X_{TS}(e^{j\omega_1})X_{TS}(e^{j\omega_2})|)$ and UCA $(|X_{CT}(e^{j\omega_1})X_{CT}(e^{j\omega_2})|)$ regions are shown in Figure 3.3(a) and (b), respectively. Figure 3.3(c) shows the ratio of contrast to tissue magnitude, i.e. $\frac{|X_{CT}(e^{j\omega_1})X_{CT}(e^{j\omega_2})|}{|X_{TS}(e^{j\omega_1})X_{TS}(e^{j\omega_2})|}$. Four distinct peaks in the 2D plane of contrast to tissue magnitude are observed at frequencies corresponding to second harmonics due to UCA, i.e. 3 MHz. Figure 3.3(d) shows the magnitude of 2D frequency response of the optimal quadratic filter $(|H_2(e^{j\omega_1},e^{j\omega_2})|)$. The magnitude of frequency responses of quadratic components from tissue $(|H_2(e^{j\omega_1},e^{j\omega_2})||X_{TS}(e^{j\omega_1})X_{TS}(e^{j\omega_2})|)$ and UCA $(|H_2(e^{j\omega_1},e^{j\omega_2})||X_{CT}(e^{j\omega_1})X_{CT}(e^{j\omega_2})|)$ regions in the (ω_1,ω_2) plane are shown in Figure 3.3(e) and (f), respectively. We can clearly see that the quadratic filter appropriately amplifies the region where UCA is higher than tissue at frequency (3,3) and (-3,-3) MHz.

Figure 3.4(a) shows a more quantitative insight of the quadratic filter in the frequency domain. Line graphs that corresponding to magnitude frequency where $f_1 + f_2 = 6$ MHz in the (ω_1, ω_2) plane of the UCA, tissue, and filter are shown using, thick, dotted, and thin lines, respectively. One can see that the filter has a high gain where UCA is higher than tissue. Figure 3.4(b) shows average spectra of data from the QB-mode image in UCA $(|Y_{CT}(e^{j\omega})|)$ and tissue $(|Y_{TS}(e^{j\omega})|)$ regions using solid and dotted lines, respectively. The intersection points between the dashed vertical line and other two horizontally spectral lines are from the integration along the diagonal line $f_1 + f_2 = 6$ MHz, i.e. $\int_0^{2\pi} \int_0^{2\pi} H_2(e^{j\omega_1}, e^{j\omega_2}) X_{CT}(e^{j\omega_1}) X_{CT}(e^{j\omega_2}) d\omega_1 d\omega_2$ and

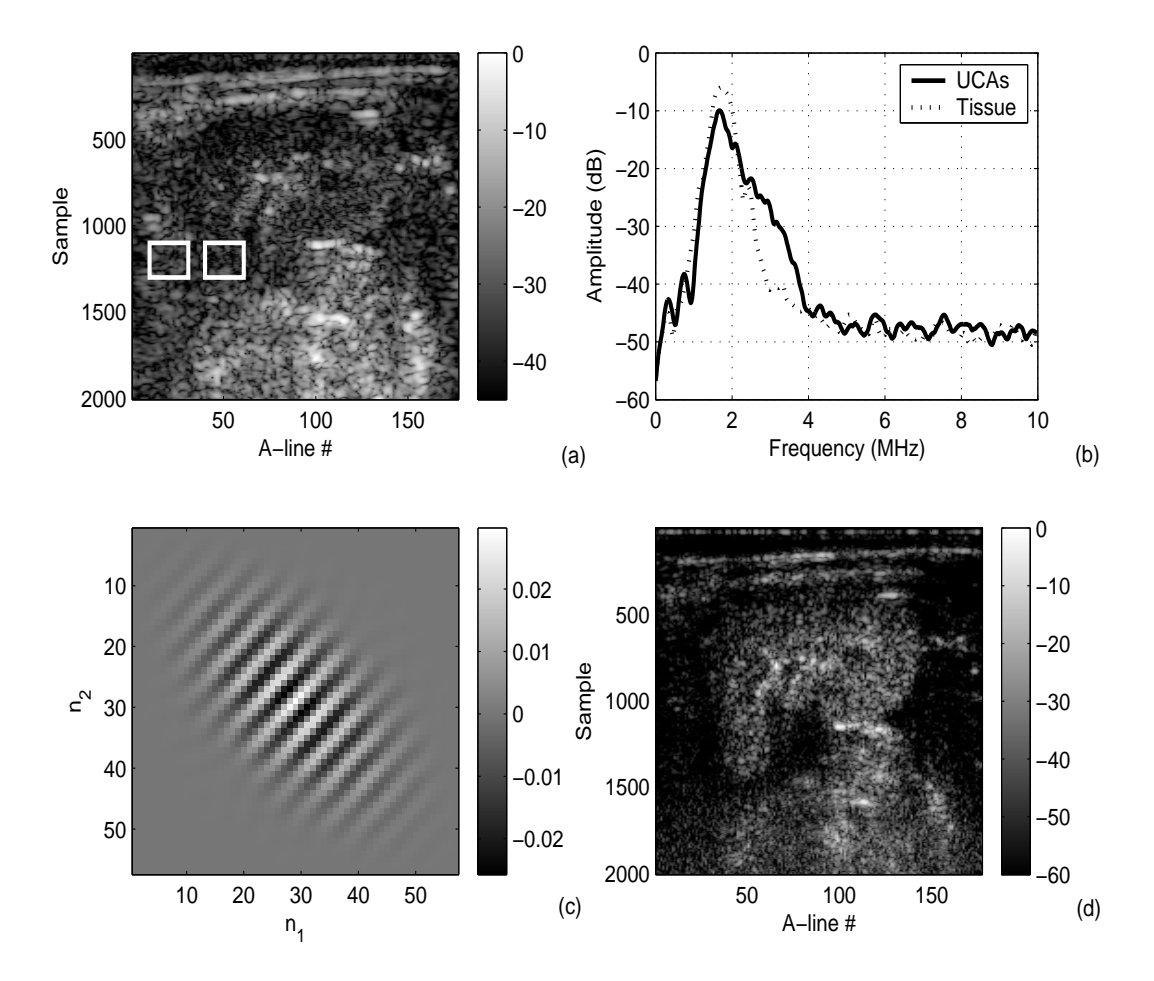


Figure 3.2: (a) B-mode image of the kidney. (b) Average spectra of RF data. Solid: $|X_{CT}(e^{j\omega})|$, Dotted: $|X_{TS}(e^{j\omega})|$. (c) The optimal quadratic filter. (d) QB-mode image.

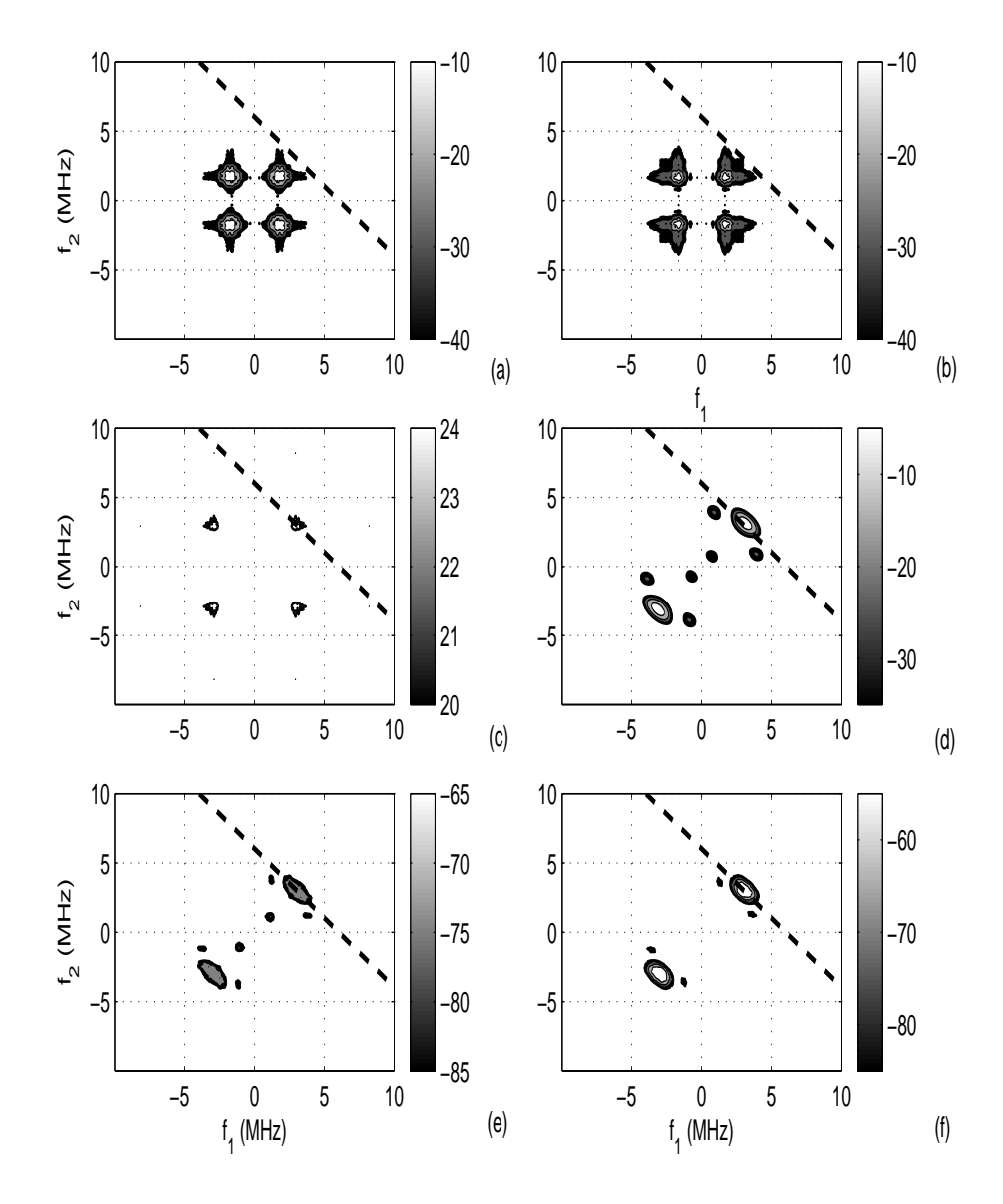


Figure 3.3: Filled contour plots of magnitude frequency responses in the (ω_1, ω_2) plane: (a) $|X_{TS}(e^{j\omega_1})X_{TS}(e^{j\omega_2})|$, (b) $|X_{CT}(e^{j\omega_1})X_{CT}(e^{j\omega_2})|$, (c) $\frac{|X_{CT}(e^{j\omega_1})X_{CT}(e^{j\omega_2})|}{|X_{TS}(e^{j\omega_1})X_{TS}(e^{j\omega_2})|}$, (d) $|H_2(e^{j\omega_1}, e^{j\omega_2})|$, (e) $|H_2(e^{j\omega_1}, e^{j\omega_2})||X_{TS}(e^{j\omega_1})X_{TS}(e^{j\omega_2})|$, and (f) $|H_2(e^{j\omega_1}, e^{j\omega_2})||X_{CT}(e^{j\omega_1})X_{CT}(e^{j\omega_2})|$. In addition, the diagonal line $f_1 + f_2 = 6$ MHz is overlaid in the (ω_1, ω_2) plane.

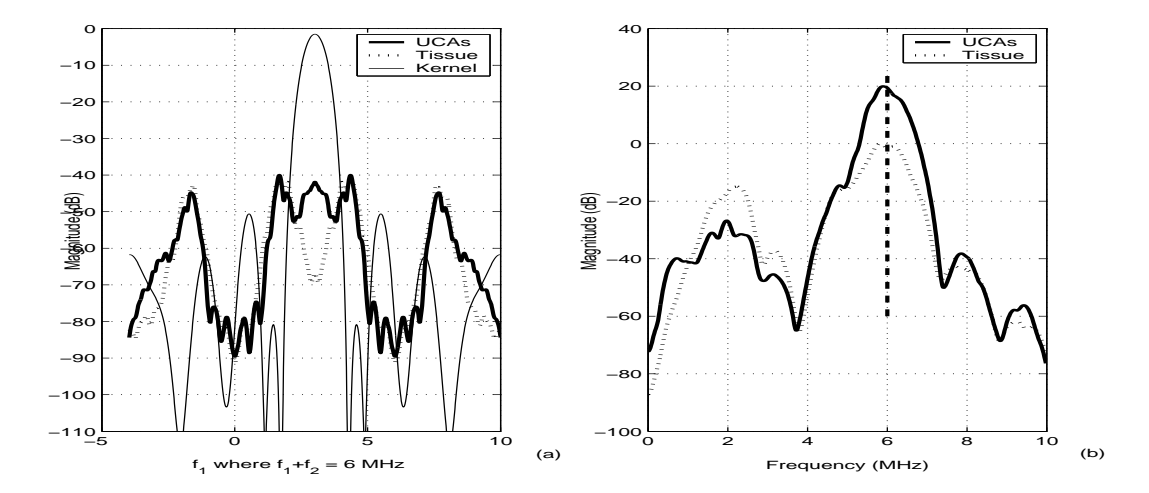


Figure 3.4: (a) Solid: $|X_{CT}(e^{j\omega_1})X_{CT}(e^{j\omega_2})|$, Dotted: $|X_{TS}(e^{j\omega_1})X_{TS}(e^{j\omega_2})|$, and Thin: $|H_2(e^{j\omega_1},e^{j\omega_2})|$ where $f_1+f_2=6$ MHz. (b) Solid: $|Y_{CT}(e^{j\omega})|$, Dotted: $|Y_{TS}(e^{j\omega})|$.

 $\int_0^{2\pi} \int_0^{2\pi} H_2(e^{j\omega_1}, e^{j\omega_2}) X_{TS}(e^{j\omega_1}) X_{TS}(e^{j\omega_2}) d\omega_1 d\omega_2 \text{ where } f_1 + f_2 = 6 \text{ MHz}.$

3.5 Discussion

We analyze frequency-domain characteristics of the quadratic filter that is able to separate quadratic components from UCA signals. QB-mode images produced using those quadratic components show significant improvement in both contrast and spatial resolution. The understanding of the quadratic filter in the frequency domain allows for the improved filter design in term of both filter size and contrast enhancement capability. Details of the new design and evaluation are presented in the next chapter.

Chapter 4

Quadratic Filter Design and Evaluation

4.1 Introduction

With the understanding of the quadratic filter (QF) in frequency domain [34], we propose a novel method to design the QF for separating quadratic components and demonstrate the preliminary evaluation [35]. The new design approach allows for two degrees of freedom in optimizing time and frequency resolution independently. That is, axial resolution can be maintained while contrast resolution is maximized. Thus, it overcomes the trade-off in time frequency resolution problem appearing in linear bandpass filtering, which has only one degree of freedom in filter optimization. For example, in order to increase contrast resolution in linear bandpass filtering, the passband width of filter must be decreased. This unavoidably degrades axial resolution. In addition, the QF designed by new proposed method can separate nonlinearity from both UCA and nonlinear propagation. In this chapter, we present the details on optimizing parameter adjustment in the QF design for achieving contrast and axial resolution simultaneously. Evaluation of the approach is demonstrated using a flow phantom target containing UCA and a quality assurance ultrasound phantom consisting of resolution targets.

4.2 Quadratic Filter Design

The quadratic image is produced using the QF output, in which the relation between RF input x(n) and QF output y(n) can be expressed as

$$y(k) = \sum_{n_1=0}^{P-1} \sum_{n_2=0}^{P-1} h(n_1, n_2) x(k - n_1) x(k - n_2),$$
(4.1)

where $h(\cdot, \cdot)$ represents the quadratic filter and P is the system memory. The quadratic image is produced by applying the optimum QF kernel to the beamformed RF data throughout the B-mode image. The input-output relation of the QF shown in Equation 5.3 in frequency domain is given by

$$Y(e^{j\omega}) = \frac{1}{2\pi} \int_0^{2\pi} \int_0^{2\pi} H(e^{j\omega_1}, e^{j\omega_2}) X(e^{j\omega_1}) X(e^{j\omega_2}) d\omega_1 d\omega_2$$
 (4.2)

under the assumption

$$\omega_1 + \omega_2 = \omega, \tag{4.3}$$

where $Y(e^{j\omega})$ is the discrete-time Fourier transform (DTFT) of y(n), $X(e^{j\omega})$ is the DTFT of x(n), and $H_2(e^{j\omega_1}, e^{j\omega_2})$ is the 2D DTFT of $h_2(\cdot, \cdot)$. Note that the observed quadratic signal component at ω is the result of the sum of mixing all frequency components ω_1 and ω_2 such that $\omega_1 + \omega_2 = \omega$ weighted by the quadratic frequency response at $\omega_1 + \omega_2 = \omega$.

We design the optimum QF for separating nonlinearity signals in frequency domain. The linear-phased QF is designed based on the sum of two 2D Gaussian filters where their centers are placed at the maximal contrast-to-tissue ratio of UCA over surrounding tissue. In the design, parameters are varied and investigated in order to achieve the best filter for enhancing imaging quality both in terms of contrast and axial resolution. In general, the frequency response of the QF from the discrete Fourier transform (DFT) can be expressed as [36]

$$H(e^{j\omega_{1k}}, e^{j\omega_{2l}}) = \sum_{n_1=0}^{N_1-1} \sum_{n_2=0}^{N_2-1} h(n_1, n_2) e^{-jn_1\omega_{1k}} e^{-jn_2\omega_{2l}}, \tag{4.4}$$

where $H(e^{j\omega_{1k}}, e^{j\omega_{2l}})$ is a 2D frequency response of the QF, $h(n_1, n_2)$ is the coefficients of the QF, N_1 and N_2 are the length of the QF on n_1 and n_2 , respectively. Our goal in

the design is to calculate coefficients of the QF, $h(n_1, n_2)$, from the frequency response given by

$$H(e^{j\omega_{1k}}, e^{j\omega_{2l}}) = G(\omega_{1k}, \omega_{2l})e^{j\phi(\omega_{1k}, \omega_{2l})}, \tag{4.5}$$

where $G(\omega_{1k}, \omega_{2l})$ represents the desired magnitude response based on the 2D Gaussian filters and $\phi(\omega_{1k}, \omega_{2l})$ is the phase response, which can be expressed as [36]

$$\phi(\omega_{1k}, \omega_{2l}) = -\frac{N_1 - 1}{2}\omega_{1k} - \frac{N_2 - 1}{2}\omega_{2l}, \tag{4.6}$$

where $\omega_{1k}=(2\pi k/M_1)-\pi$, $k=0,1,...,M_1-1$ and $\omega_{2l}=(2\pi l/M_2)-\pi$, $l=0,1,...,M_2-1$. We use the QF size $N_1=N_2=N$. As a result, the phase delay of the signal output is (N-1)/2.

It has been shown that the passband of optimum QF situates in 2D frequency plane where the contrast-to-tissue ratio of UCA over surrounding tissue is maximal [34]. Based on this guidance, the magnitude frequency response of the QF can be designed using the sum of 2D Gaussian filters, which is given by

$$G(\omega_{1k}, \omega_{2l}) = \frac{G_1(\omega_{1k}, \omega_{2l}) + G_2(\omega_{1k}, \omega_{2l})}{\max\{G_1 + G_2\}},$$
(4.7)

where

$$G_i(\omega_{1k},\omega_{2l}) =$$

$$\exp\{-[A(\omega_{1k} - \omega_{ai})^2 + B(\omega_{1k} - \omega_{ai})(\omega_{2l} - \omega_{bi}) + C(\omega_{2l} - \omega_{bi})^2]\},\tag{4.8}$$

for i = 1, 2 with:

$$A = \left(\frac{\cos\theta}{\sigma_x}\right)^2 + \left(\frac{\sin\theta}{\sigma_y}\right)^2 \tag{4.9}$$

$$B = -\frac{\sin 2\theta}{\sigma_x^2} + \frac{\sin 2\theta}{\sigma_y^2} \tag{4.10}$$

$$C = \left(\frac{\sin \theta}{\sigma_x}\right)^2 + \left(\frac{\cos \theta}{\sigma_y}\right)^2. \tag{4.11}$$

The coefficient $(\omega_{ai}, \omega_{bi})$ is the center of Gaussian filter, σ_x and σ_y are constants that define the passband width along two frequency directions, and θ is the rotation angle.

After we derive the frequency response $H(e^{j\omega_{1k}}, e^{j\omega_{2l}})$ from Equation 4.5, we can obtain the coefficients $h(n_1, n_2)$ using the inverse discrete Fourier transform (IDFT). When the linear-phased QF based on the 2D Gaussian filters in the frequency domain is formed, the filter coefficients can be obtained using the IDFT as follows,

$$h(n_1, n_2) = \frac{1}{M_1 M_2} \sum_{k=0}^{M_1 - 1} \sum_{l=0}^{M_2 - 1} H(e^{j\omega_{1k}}, e^{j\omega_{2l}}) e^{jn_1\omega_{1k}jn_2\omega_{2l}}, \tag{4.12}$$

where M_1 and M_2 are the number of point used in IDFT along ω_{1k} and ω_{2l} , respectively. In this paper, we use $M_1 = M_2 = M$.

Figure 4.1 shows a flowchart of the quadratic imaging generation for the design approach. First, we set an initial value for the size of the QF, N, and the number of point used in the DFT and IDFT, M. Next, parameters $\sigma_x, \sigma_y, \theta$ and two centers of 2D Gaussian filters are chosen. Then, we form the QF in frequency domain and take IDFT to obtain filter coefficients. We measure the difference of the desired QF and the QF from IDFT using normalized mean square error (NMSE), which is given by

$$NMSE = \frac{\sum \sum (\hat{G} - G)^2}{\sum \sum G^2}.$$
 (4.13)

If the NMSE is higher than the value that we define (ϵ) , we increase the kernel size N in order to reduce the NMSE until we obtain the defined NMSE. The QF based on the 2D Gaussian filters with optimum parameters is capable of enhancing UCA components while suppressing tissue signals. We use signal outputs from the QF to produce a gray-level image, which has better quality for medical diagnosis.

Figure 4.2 shows an example of 3D magnitude frequency response of the optimum QF in frequency domain resulting from Equation 4.8 and its corresponding kernel in time domain. In addition, their shapes and characteristics in 2D are shown in Figure 4.3. An important advantage of our proposed design is that time-frequency resolution can be determined independently. That is, a narrower passband in major axis (σ_y) gives higher contrast resolution and a wider passband in minor axis (σ_x) provides finer axial resolution. On the other hand, for the optimum QF in the time domain, the time and

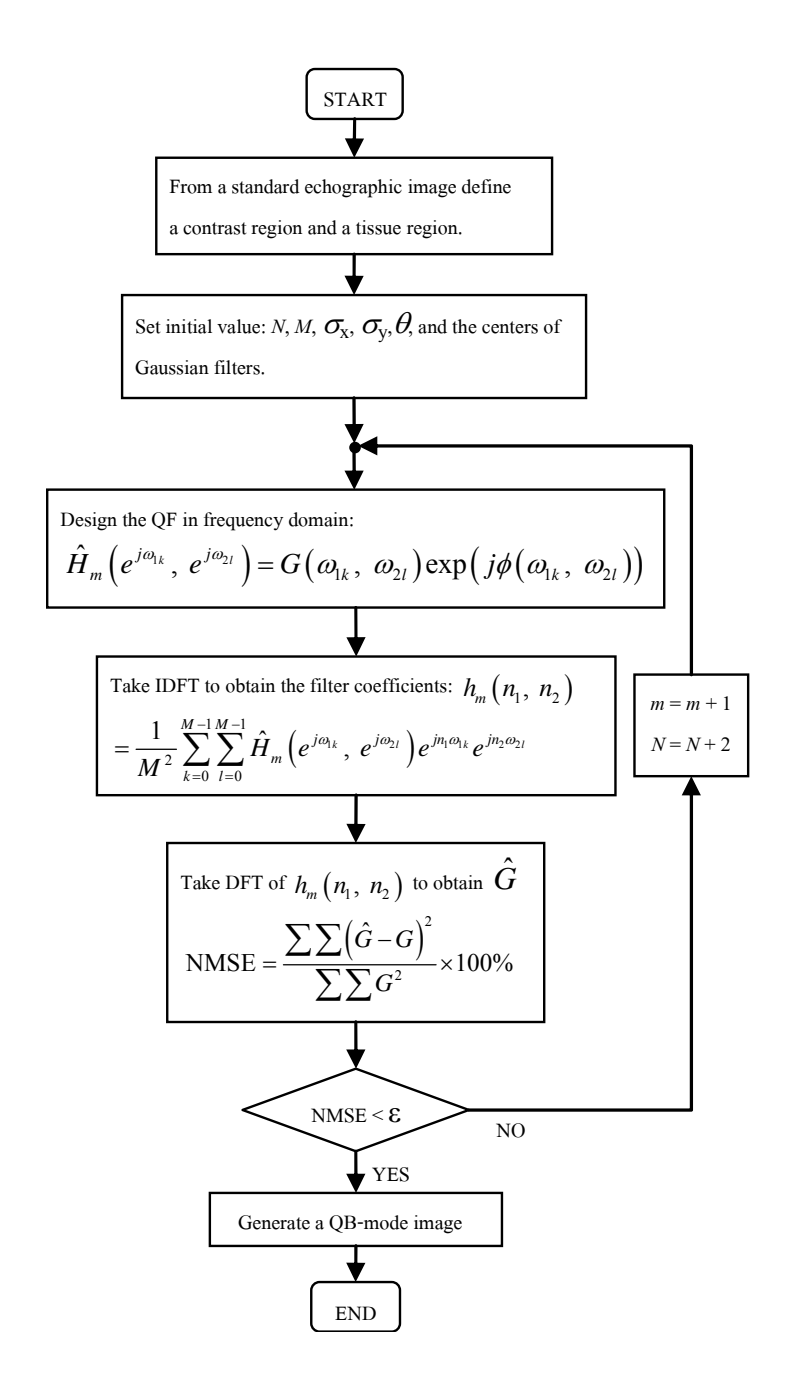


Figure 4.1: A flowchart of the algorithm for QF design.

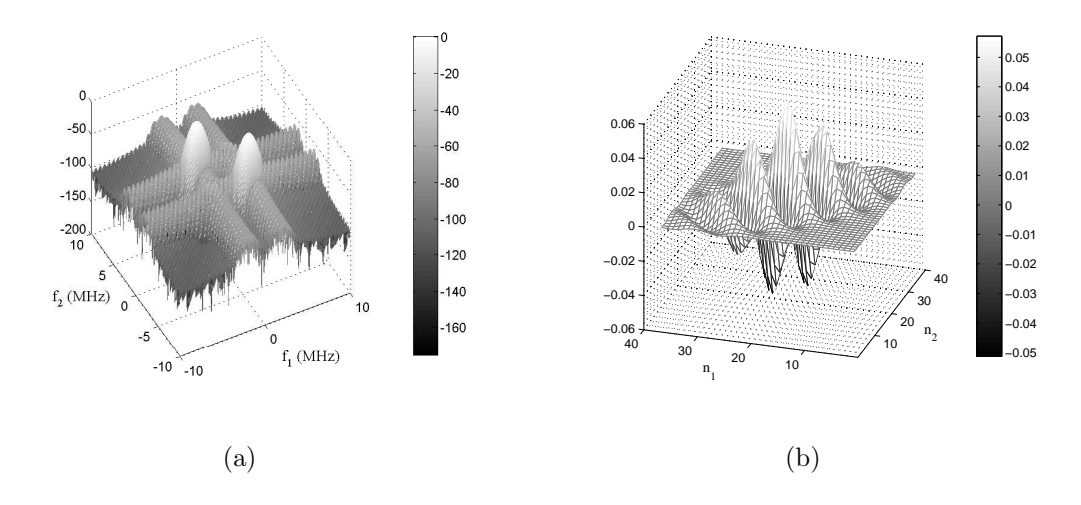


Figure 4.2: (a) 3D magnitude frequency response of the QF in frequency domain. (b) The corresponding QF kernel in time domain.

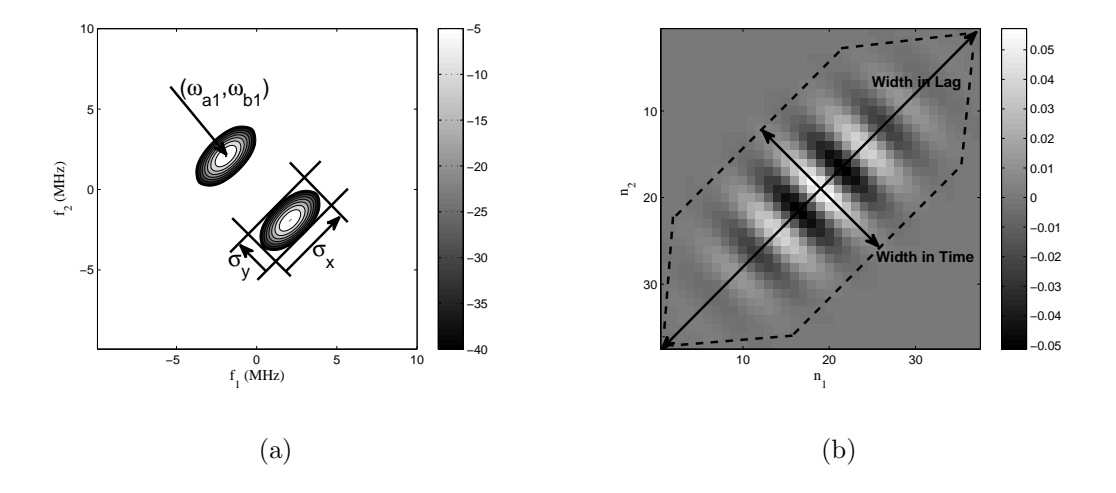


Figure 4.3: (a) 2D magnitude frequency response of the QF in frequency domain. (b) The corresponding QF kernel in time domain.

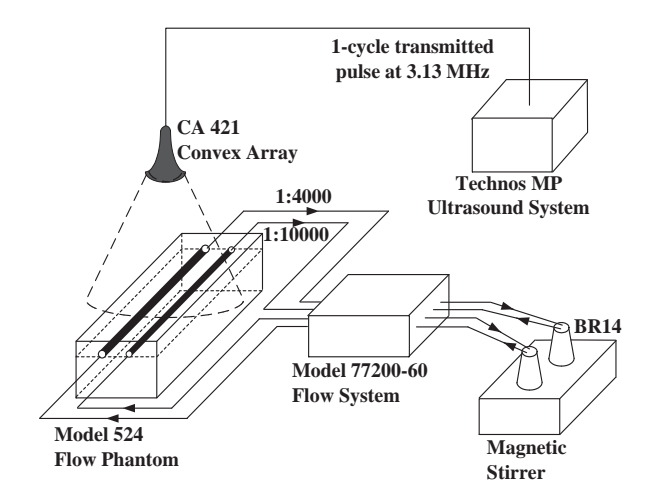


Figure 4.4: The imaging setup for the flow phantom.

frequency resolution of the QF rely on the width of the region where filter coefficients are nonzero in major (time) and minor (lag) orientations, respectively. In other words, a narrower width in time gives finer axial resolution and a wider width in lag provides higher contrast resolution. Consequently, the kernel with the best resolution in both time and frequency must have nonzero elements only along the minor orientation [37].

4.3 Materials and Methods

The objective of the flow phantom experiment is to demonstrate the use of quadratic imaging with transmit pulses optimized for maximum resolution (as in conventional B-mode) and examining the resulting CTR enhancement. In this experiment, we used wideband transmission (one cycle) operating at the transducer center frequency.

The setup shown in Figure 4.4 was used in obtaining images of a flow phantom (ATS Laboratories Model 524) containing flow channels embedded in rubber-based tissue mimicking material. The flow phantom was connected to a flow system with a roller pump (Cole-Parmer Instrument Model 77200-60). Subsequently, the diluted contrast agents was circulated and constantly stirred in beakers using a magnetic plate stirrer (Corning EW-84303-20). The contrast agent, BR14 (Bracco Research), was used. BR14

is a new experimental agent that consists of high molecular weight gas bubbles encapsulated by a flexible phospholipid shell. While UCA with 1:4000 dilution was circulated through the 6-mm channel, UCA with 1:10000 dilution was circulated through the 4-mm channel.

RF data were recorded and saved for off-line processing by the Technos MPX ultrasound system (ESAOTE) with a convex array probe (ESAOTE CA421) located perpendicularly to the flow channels. In addition, the probe position was slightly tilted to avoid strong specular reflections. RF data were acquired with 16-bit resolution at 20-MHz sampling frequency without time gain control (TGC) compensation. A one-cycle pulse at 3.13 MHz was transmitted to form standard B-mode images with a mechanical index (MI) of 0.279. For each flow condition, twenty frames of RF data from standard B-mode images were collected in 10 s.

4.4 Results

4.4.1 Flow Phantom

The B-mode image in Figure 4.5 (top left) shows that echogenicity of the 6-mm channel is significantly increased to produce a positive contrast, while the echogenicity of the 4-mm channel is slightly higher than its surroundings. This is in line with the relative difference in concentration. That is, the strength of echoes from UCA with 1:4000 dilution in the 6-mm flow channel (CTR = 5.5 dB) is higher than those from UCA with 1:10000 dilution in the 4-mm flow channel (CTR = 2.9 dB).

Figure 4.6(a) shows that the average spectra of raw RF data in the 6-mm flow channel (Solid) are broader than those from tissue regions (Dotted). The most visible enhancement occurs around 2 MHz. This is probably due to the natural resonance of the UCA and could be a mix of linear and nonlinear components. Figure 4.6(b) shows a filled contour plot of the ratio of contrast to tissue magnitude, i.e.,

$$\frac{|X_{CT}(e^{j\omega_1})X_{CT}(e^{j\omega_2})|}{|X_{TS}(e^{j\omega_1})X_{TS}(e^{j\omega_2})|},$$

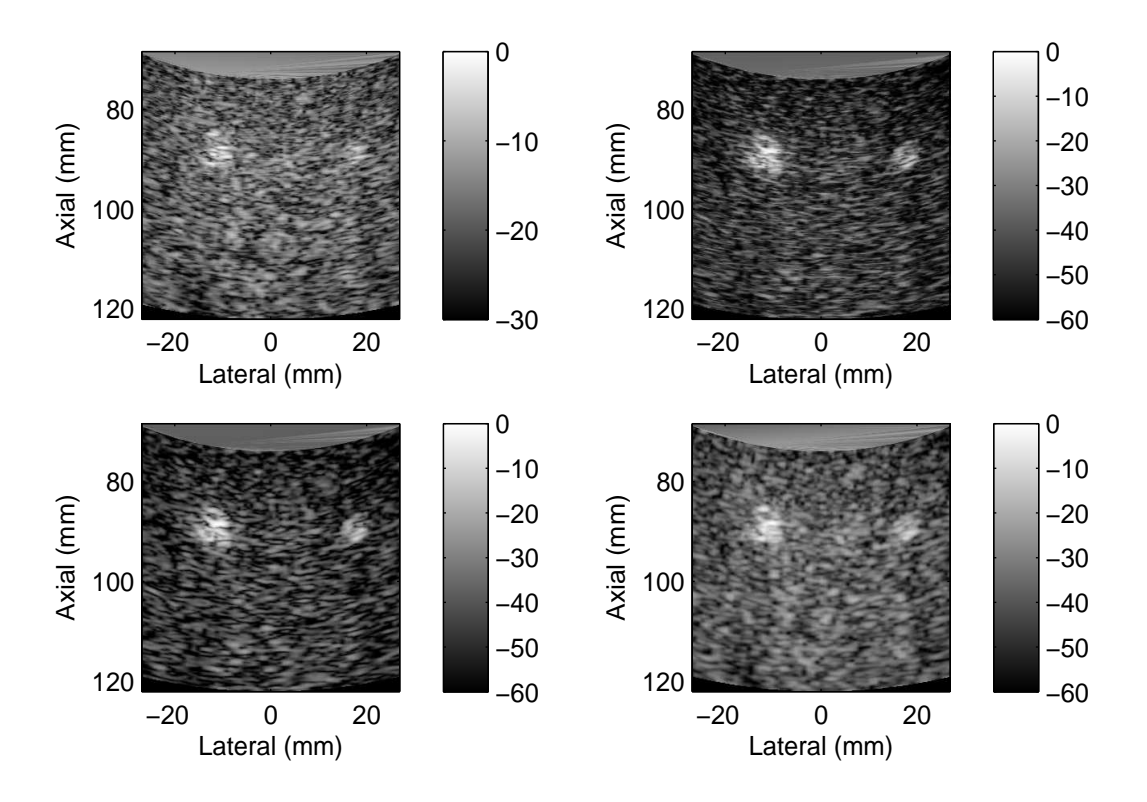


Figure 4.5: Top Left: B-mode image of a flow phantom. Images from the QF1, QF2, and QF3 are shown at top right, bottom left, and bottom right, respectively.

in the (ω_1, ω_2) plane. Two distinct peaks in 2D plane of contrast to tissue magnitude in major axis are observed at frequencies (-2,2) and (2,-2) MHz. These two pair of frequencies are used as the centers of two 2D Gaussian functions.

We compare the effects of QF parameters on contrast and axial resolution of ultrasound image using three settings. Figure 4.7 (right) shows the magnitude of 2D frequency responses of three QFs under investigation. The centers of Gaussian function are at frequency (-2, 2) and (2, -2) MHz, where their contrast to tissue magnitude in the 2D frequency response are maximal. Other parameters, i.e., $(\sigma_x, \sigma_y, \theta)$ for the QF1, QF2, and QF3 are $(1.1, 0.55, -\pi/4)$, $(0.55, 0.55, -\pi/4)$ and $(0.55, 1.1, -\pi/4)$, respectively. The QF spreads in major and minor axes are varied for demonstrating their effects on imaging quality. Figure 4.7 (left) shows the corresponding coefficients of the QFs. The size of the QF1, QF2, and QF3 in time domain are 37, 47, and 37, respectively. Note that the

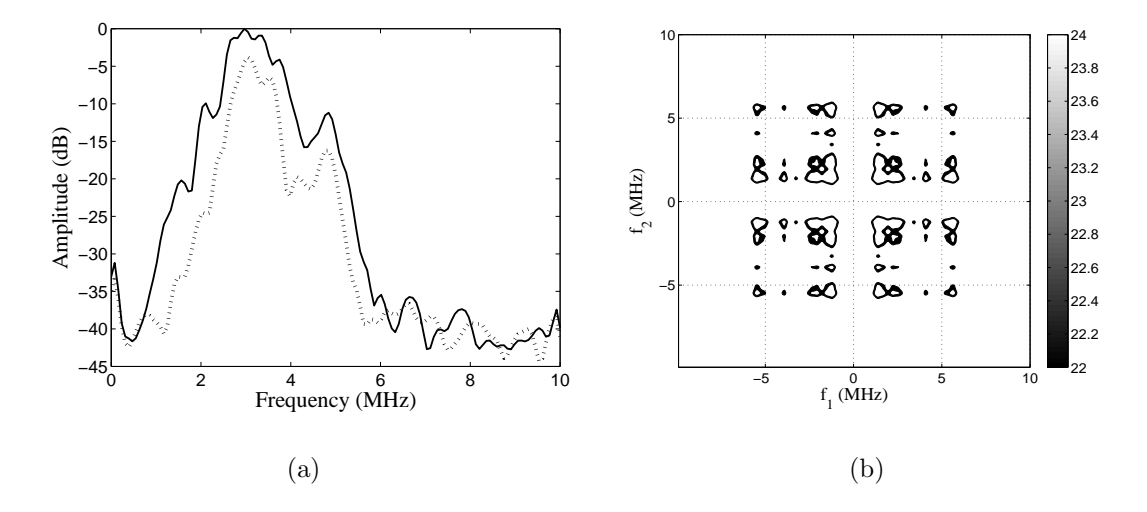


Figure 4.6: (a) Average power spectra from the UCA (solid) and tissue (dotted) regions in B-mode imaging. (b) Contrast to tissue ratio in 2D magnitude frequency response.

kernel size is in the range of acceptable real time implementation.

The QF images produced using QF1, QF2, and QF3 are shown in Figure 4.5. The contrast enhancement of QF2 image is comparable to that from the optimum QF1 image due to their similar passband width in major axis (σ_y). However, there is loss of axial resolution in the image from QF2, which can be clearly seen using resolution targets in a quality assurance phantom shown in next section. This is due to the fact that the QF1 has a wider passband (σ_x) in minor axis compared to the QF2 resulting in finer axial resolution. In addition, we can see that the quadratic image from the optimum QF1 shows significant enhancement of both flow channels compared to corresponding the B-mode image without the sacrifice of spatial resolution. This visible enhancement agrees with CTR computed from the high (1:4000 dilution) region in the large flow channel of QF1, i.e., 23.8 dB. On the other hand, the CTR values of quadratic images resulting from the QF2 and QF3 from same region of interest in the large flow channel are 25.2 and 16.1 dB, respectively. Low CTR value in the QF3 is caused by its wide passband width in major axis.

4.4.2 Quality Assurance Phantom

Additional study on axial resolution is carried out using the image from an ultrasound quality assurance phantom. Figure 4.8 (top left) shows the B-mode image of the quality assurance phantom, which is used as a baseline for comparison. The QF images resulting from the same QF kernels used to generate QF images of the flow phantom in Figure 4.5 are shown in Figure 4.8. Visual comparisons of specular reflections from point objects (i.e., resolution targets) between B-mode and QF1 quadratic image shown in Figure 4.8 (top right) indicate no apparent loss of spatial resolution. In addition, visualization of other objects is observable in the QF1 image, i.e., cystic targets, high contrast targets, and high density targets.

Figure 4.9 (top) shows axial lines through the center of quality assurance phantom. The thick, thin, and dash lines are from the QF1, QF2, and QF3, respectively. The resolution targets at the distance from 93 to 99 mm are shown in Figure 4.9 (bottom) for better visualization. It can be seen that the axial resolution of QF1 image is better than that from the QF2 and QF3 due to its wide passband in minor axis. Based on this demonstrating results, we can see that the QF with wide bandwidth in minor axis, i.e., cross-diagonal orientation, provides the image with better axial resolution.

4.5 Discussion

We present the novel design of optimum quadratic filter (QF) for separating nonlinearity in pulse-echo ultrasound signals. In the design, time and frequency resolution can be independently determined based on the spread of filter passband in minor (cross-diagonal) and major (diagonal) axes, respectively. While the wider passband in minor axis provide finer axial resolution, the narrower passband in major axis provide higher contrast resolution. Evaluations of the approach on a flow phantom target and an ultrasound quality assurance phantom are performed. Results show that the proposed method allows for obtaining the quadratic image with high contrast resolution with no apparent loss in

axial resolution. In addition, the proposed design approach can be extended to simultaneously separate multiple harmonics for maximizing nonlinearity detection. Results from ongoing research is going to be reported in the near future.

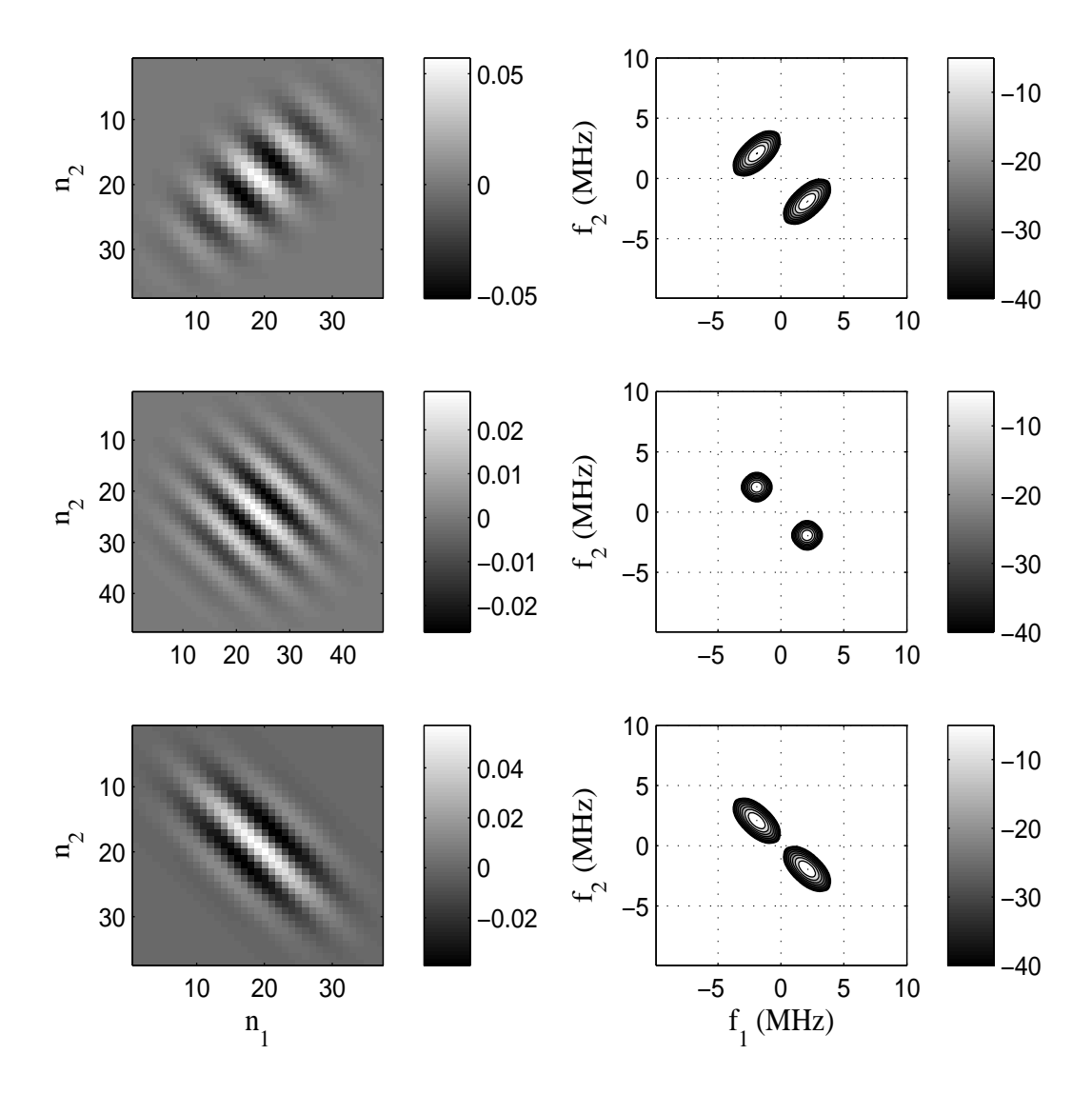


Figure 4.7: Left: Coefficients of the QF1, QF2, and QF3 are shown from top to bottom rows, respectively. Right: The corresponding magnitude of 2D frequency responses of the QF in left column.

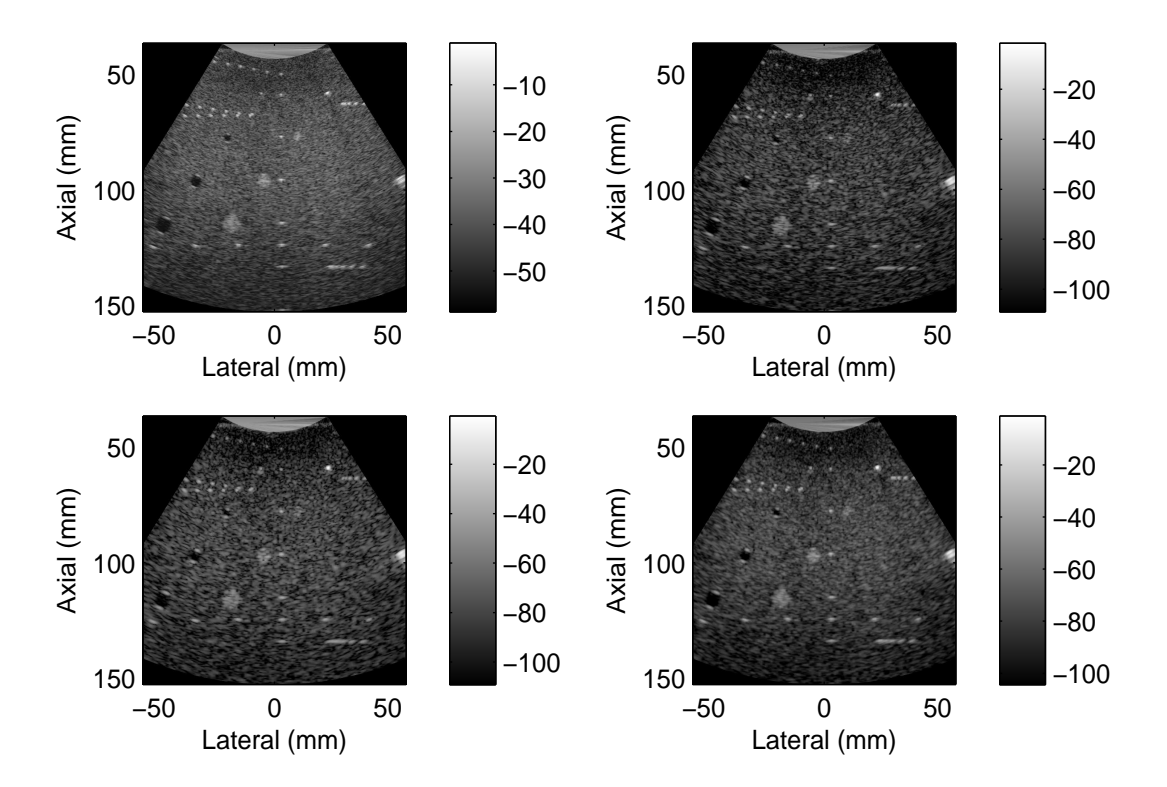
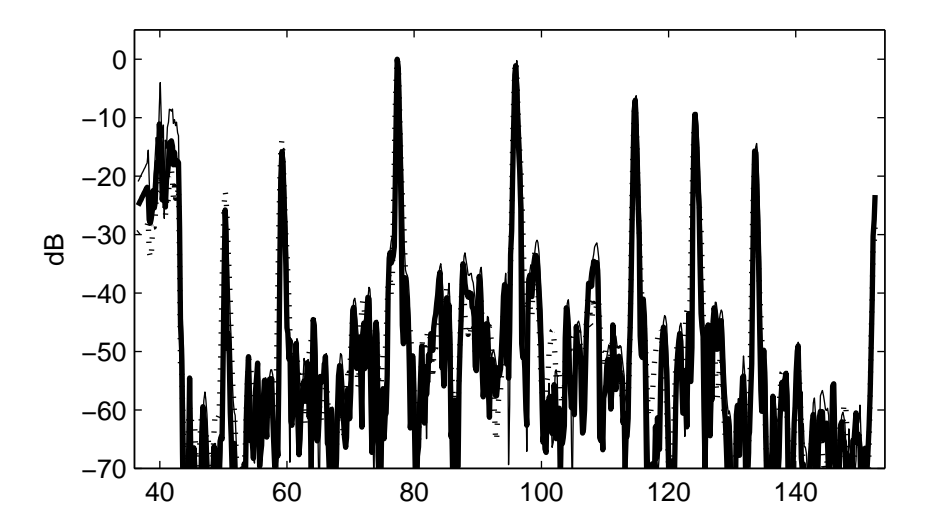


Figure 4.8: Top left: B-mode image of a quality assurance phantom. The images from the QF1, QF2, and QF3 are shown at top right, bottom left, and bottom right, respectively.



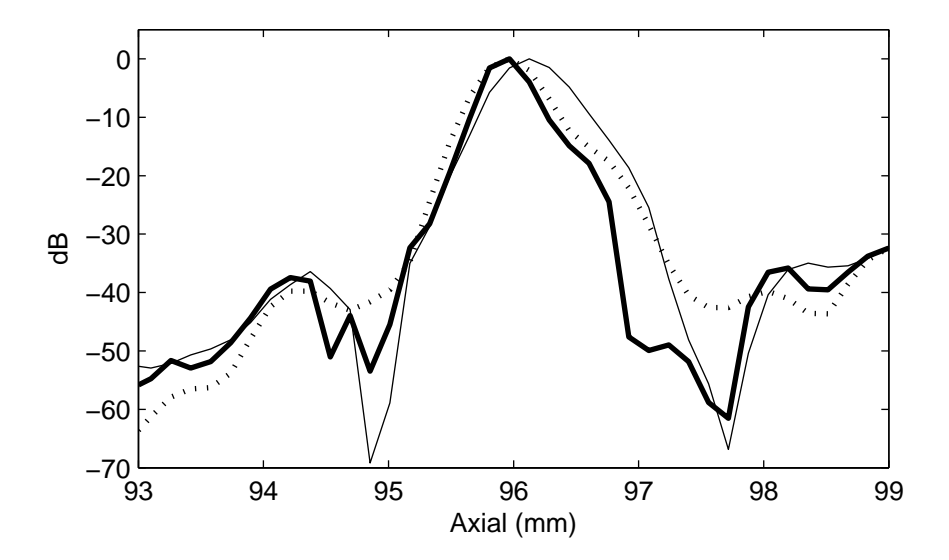


Figure 4.9: Top: Axial lines through the center of the quality assurance phantom. Thick: QF1. Thin: QF2. Dash: QF3. Bottom: Corresponding axial lines in the distance between 93 and 99 mm.

Chapter 5

Second-Order Volterra System Identification

5.1 Introduction

The success of Volterra filters as nonlinear models for other physical systems provides the inspiration for applying them with nonlinear ultrasound problems. The application of Volterra filters based on its prediction model have been shown in [38]. Imaging results show the improvement in contrast resolution with no loss of spatial resolution. This chapter investigates the use of a second-order Volterra filter (SVF) model in the aspect of system identification for separating the linear and nonlinear components of the beamformed radio frequency (RF) data in pulse-echo ultrasonic imaging.

5.2 Theory

5.2.1 Nonlinear Pulse-Echo System

In this section, a model to produce RF lines from a nonlinear pulse-echo system (NPS) is presented. The RF signal resulting from the interaction of the transmitted pulse and a particle can be expressed as

$$s(t) = \frac{\rho}{2c} \frac{\partial^2 v(t)}{\partial t^2} * h_t(r, t) * f_{sc}(r, t) * h_r(r, t), \tag{5.1}$$

where * denotes a convolution, v is the electromechanical conversion, ρ is the density, and c is the sound speed in the medium. h_t and h_r represent spatial impulse responses in

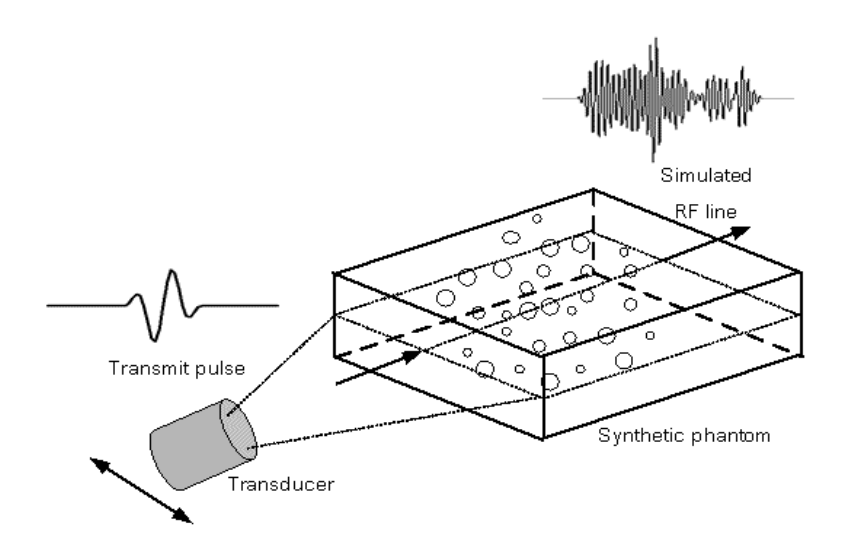


Figure 5.1: A diagram showing the generation of an RF line from the NPS.

transmission and in reception modes that relate to the transducer geometry, respectively. Both h_t and h_r are computed using the Field II program [39], which is capable of generating linear pressure fields from a wide variety of ultrasound transducers. f_{sc} is the temporal impulse response of the particle. In a viewpoint of practical medical ultrasonic diagnosis of human body, the RF signal resulting from Equation 5.1 may simulate human tissues with different nonlinearity parameter B/A, such as fatty and liver tissues, by utilizing the Khokhlov-Zabolotskaya-Kuznetsov (KZK) equation [40].

A nonlinear mathematical model for the particle is appropriately chosen to match with the medium. For example, if the particle is a microbubble contrast agent, the modified Herring equation [41] is able to predict echoes from radial oscillations of a single encapsulated bubble. An RF line is obtained by a weighted addition of RF signals from all particles in the region of interest. A diagram showing the generation of an RF line is shown in Figure 5.1.

5.2.2 Volterra Filter

While a Taylor series is used to model a nonlinear system without memory, a nonlinear system with memory can be described using its extension form, a Volterra series. The relationship between the output and input of a discrete Volterra series, also referred to as a Volterra filter or a polynomial filter, can be written in the form [42]

$$y(n) = h_0 + \sum_{p=1}^{\infty} \sum_{k_1 = -\infty}^{\infty} \cdots \sum_{k_p = -\infty}^{\infty} h_p(k_1, ..., k_p) \prod_{q=1}^{p} x(n - k_q),$$
 (5.2)

where y(n) is the output, x(n) is the input, and $h_p(n_1, ..., n_p)$ represents the pth-order Volterra kernel. Generally, the Volterra kernel can be complex values. In this paper, however, only the kernel consisting of real values is considered. In addition, both input and output are real. The value of h_0 is also assumed to be zero.

For simplicity and without loss of generality, this paper examines properties and interpretations of the Volterra filter using its truncated version of order 2, i.e. a second-order Volterra filter (SVF). In practice, a output of the SVF from a causal system with a finite memory can be expressed as:

$$y(n) = \sum_{k_1=0}^{N-1} h_1(k_1)x(n-k_1) + \sum_{k_1=0}^{N-1} \sum_{k_2=0}^{N-1} h_2(k_1, k_2)x(n-k_1)x(n-k_2),$$
 (5.3)

where $h_1(n)$ and $h_2(n_1, n_2)$ represent the first- and the second-order Volterra kernels, respectively.

Two important properties resulting from the structure of the SVF are as follows: First, the SVF output depends linearly on elements of Volterra kernels. This property plays an important role in analyzing quadratic filters, deriving adaptive algorithms, etc. One of the most interesting advantage is that it allows a straightforward extension of adaptive algorithms for linear filters to those for Volterra filters. Second, the SVF output is the sum of multidimensional convolutions of the products of input with Volterra kernels. It can be clearly seen from Equation 5.3 that while the linear component (the first term on the right hand side) is determined from the convolution of x(n)with $h_1(n)$, the quadratic component (the second term on the right hand side) can be interpreted as a two-dimensional convolution of $x(n_1)x(n_2)$ with $h_2(n_1, n_2)$. In fact, the first-order Volterra kernel is also known as a linear impulse response as in a linear time-invariant discrete-time system. Therefore, by analogy with the linear impulse response, the second-order Volterra kernel can be considered as a second-order impulse response. This property allows for the analysis and design of Volterra filters in the frequency domain.

The discrete-time Fourier transform (DTFT) of the SVF system obtained by applying the Fourier transform both sides of Equation 5.3 is given by

$$Y(e^{j\omega}) = H_1(e^{j\omega})X(e^{j\omega}) + \frac{1}{2\pi} \int_0^{2\pi} H_2(e^{j\omega_1}, e^{j(\omega - \omega_1)})X(e^{j\omega_1})X(e^{j(\omega - \omega_1)})d\omega_1,$$
 (5.4)

where $X(\cdot)$ and $Y(\cdot)$ denote the Fourier transform of the input and output, and $H_1(\cdot)$ and $H_2(\cdot, \cdot)$ represent the linear and quadratic transfer functions, respectively. The linear term (the first term on the right hand side) implies that components of the input frequency are either amplified or suppressed by the corresponding gain from the linear frequency response. In the quadratic term (the second term on the right hand side), however, the multiplication of inputs in time domain $[x(n_1)x(n_2)]$ results in the convolution in frequency domain (condition $\omega_1 + \omega_2 = \omega$). Accordingly, all components at the input frequency ω_1 and ω_2 that satisfy the condition $\omega_1 + \omega_2 = \omega$ =constant contribute to the output frequency ω .

5.2.3 Identification of the SVF Model

In order to estimate the NPS using the SVF, system identification is needed as shown by the diagram in Figure 5.2. The identification problem is to find the first- and second-order Volterra kernels when input and output are known. This section presents the identification approach based on a digital method of modeling quadratically nonlinear systems with general random input [43]. A unique feature of this identification technique is that it does not require a zero-mean Gaussian random input like other methods. Consequently, this allows for a class of pseudorandom binary sequences (e.g., Barker

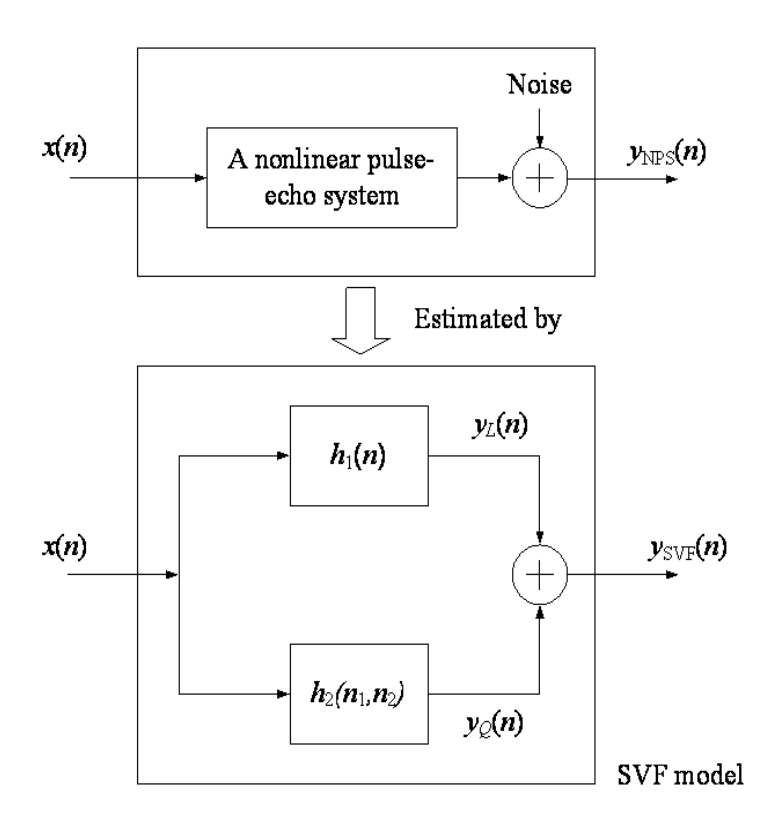


Figure 5.2: Identification of the NPS using the SVF model.

codes or maximum length sequences) that are readily available in many ultrasound and RADAR imaging systems.

The frequency response of the SVF system shown in Equation (5.4) can be represented in the discrete domain as

$$Y(f_k) = H_1(f_k)X(f_k) + \sum_{\substack{i,j = -(M-1)\\i+j=k}}^{M} H_2(f_i, f_j)X(f_i)X(f_j),$$
(5.5)

where $Y(f_k)$ and $X(f_k)$ are the Discrete Fourier transforms (DFTs) determined from a finite number (2M) of observations of the output and input sequences, respectively. In addition, the unknown variables $H_1(f_k)$ and $H_2(f_i, f_j)$ are sampled from the linear and quadratic frequency responses at a discrete set of frequencies $(f_n = n/(2M), n =$ $-M+1, \ldots, -1, 0, 1, \ldots, M)$. In order to simplify the notation, $Y(f_k)$ will be represented by $Y(k), X(f_k)$ by X(k), etc.

For real-valued data, the output frequency response has the following symmetric property: $Y(k) = Y^*(-k)$. Consequently, the expansion of Y(k) in Equation 5.5 can be sufficiently considered for only nonnegative frequency components $(k \ge 0)$. By recognizing these facts, Equation 5.5 can be rewritten as

$$Y(k) = H_1(k)X(k)$$

$$+ H_2(k - M, M)X(k - M)X(M) + \dots + H_2(0, k)X(0)X(k)$$

$$+ H_2(1, k - 1)X(1)X(k - 1) + \dots + H_2(k - 1, 1)X(k - 1)X(1)$$

$$+ H_2(k, 0)X(k)X(0) + \dots + H_2(M, k - M)X(M)X(k - M).$$
 (5.6)

Without loss of generality, the quadratic kernel is assumed to be diagonally symmetric, i.e. $h_2(n_1, n_2) = h_2(n_2, n_1)$. As a result, the quadratic frequency response satisfies the following symmetric properties: $H_2(i, j) = H_2(j, i)$ and $H_2(-i, -j) = H_2^*(i, j)$, where * denotes the complex conjugate. In other words, the quadratic transfer function is symmetric along a cross-diagonal direction and complex conjugate symmetric along a diagonal direction. This symmetry allows frequency components in the dashed zone of Figure 5.3 to specify $H_2(i, j)$ everywhere. The combination of terms in Equation 5.6

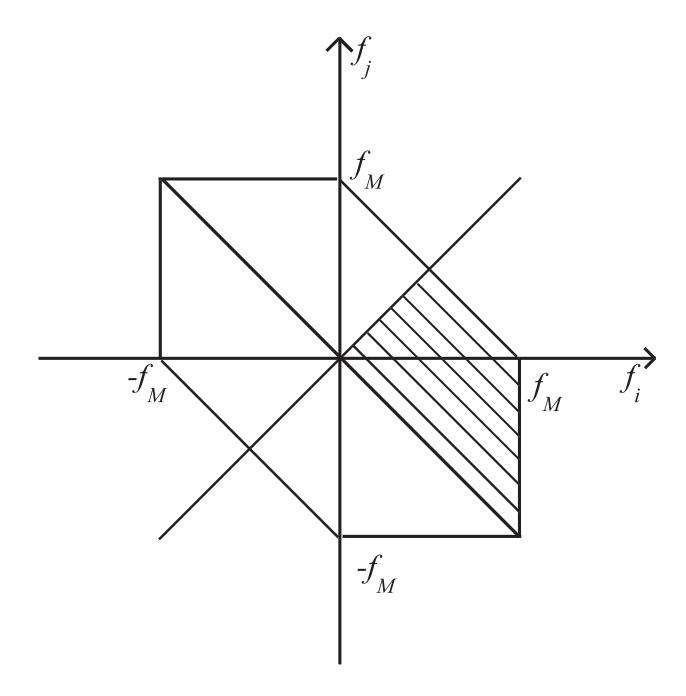


Figure 5.3: Two-dimensional frequency plane of the quadratic kernel.

using the symmetric property $H_2(i,j) = H_2(j,i)$ leads to a new compact form, which can be expressed as

$$Y(k) = \begin{cases} H_1(k)X(k) + 2[H_2(\frac{k+1}{2}, \frac{k-1}{2})X(\frac{k+1}{2})X(\frac{k-1}{2}) + \cdots \\ + H_2(M, k - M)X(M)X(k - M)], \text{ for } k \text{ odd} \end{cases}$$

$$Y(k) = \begin{cases} H_1(k)X(k) + H_2(\frac{k}{2}, \frac{k}{2})X(\frac{k}{2})X(\frac{k}{2}) & . \\ + 2[H_2(\frac{k}{2} + 1, \frac{k}{2} - 1)X(\frac{k}{2} + 1)X(\frac{k}{2} - 1) + \cdots \\ + H_2(M, k - M)X(M)X(k - M)], \text{ for } k \text{ even} \end{cases}$$

$$(5.7)$$

Using vector form, Equation 5.7 can be written as follows:

$$Y(k) = \mathbf{x}^T \mathbf{h},\tag{5.8}$$

where the superscript T represents transpose,

$$\mathbf{h}^{T} = \begin{cases} \left[H_{1}(k), \ 2H_{2}(\frac{k+1}{2}, \frac{k-1}{2}), \ \cdots, \ 2H_{2}(M, k-M) \right], \text{ for } k \text{ odd} \\ \left[H_{1}(k), \ H_{2}(\frac{k}{2}, \frac{k}{2}), \ 2H_{2}(\frac{k}{2} + 1, \frac{k}{2} - 1), \ \cdots, \ 2H_{2}(M, k-M) \right], \text{ for } k \text{ even,} \end{cases}$$
(5.9)

and

$$\mathbf{x}^{T} = \begin{cases} \left[X(k), \ X(\frac{k+1}{2})X(\frac{k-1}{2}), \ \cdots, \ X(M)X(k-M) \right], \text{ for } k \text{ odd} \\ \left[X(k), \ X(\frac{k}{2})X(\frac{k}{2}), \ X(\frac{k}{2}+1)X(\frac{k}{2}-1), \ \cdots, \ X(M,k-M) \right], \text{ for } k \text{ even.} \end{cases}$$
(5.10)

To solve for the \mathbf{h} , both sides of Equation 5.8 are multiplied from the left by \mathbf{x}^* and then an expected value is taken. The resulting equation can be expressed as

$$E\left[\mathbf{x}^*Y(k)\right] = E\left[\mathbf{x}^*\mathbf{x}^T\right]\mathbf{h},\tag{5.11}$$

where $E[\cdot]$ is the expectation operator. Equation (5.11) is a system of linear equations, which can be solved uniquely if $\left\{E\left[\mathbf{x}^*\mathbf{x}^T\right]\right\}^{-1}$ exists. The vector \mathbf{h} is given by

$$\mathbf{h} = \left\{ E \left[\mathbf{x}^* \mathbf{x}^T \right] \right\}^{-1} E \left[\mathbf{x}^* Y(k) \right]. \tag{5.12}$$

To obtain the values of the frequency response, Equation 5.12 is solved repeatedly for k = 0, ..., M. For the quadratic frequency response, the unknown variables are solved along the diagonal line $f_i + f_j = f_k$ in the dashed zone of the two-dimensional (2D) frequency plane shown in Figure 5.3. In addition, the values outside the dashed zone in the 2D frequency plane are obtained using the symmetric property of $H_2(f_i, f_j)$. After the linear and quadratic frequency responses are determined, inverse discrete Fourier transforms (IDFTs) are applied to obtain the linear and quadratic kernels.

5.2.4 Regularization

When Equation 5.12 was solved for the case of binary pseudorandom input sequences, the original algorithm calls for a full set of M/2 independent input sequences to insure a stable inverse. However, the use of regularized solution to Equation 5.12 using the pseudoinverse with a minimum set of training sequences have been tested. Robust estimates of the SVF coefficients were obtained using a small set of training sequences. This is important for a variety of imaging scenarios. For instance, high frame rate imaging where tens of training sequences cannot be afforded to send. Another example is imaging microbubble contrast agents where the time-invariance of the system holds for a

few milliseconds requiring system identification to be complete using a few transmissions.

Details of regularization are as follows.

Equation 5.12 can be expressed in the matrix form

$$\mathbf{h} = \mathbf{G}^{-1}\mathbf{f},\tag{5.13}$$

where the vector \mathbf{f} and the matrix \mathbf{G} are defined as

$$\mathbf{f} = E[\mathbf{x}^*Y(k)]$$

and

$$\mathbf{G} = E\left[\mathbf{x}^*\mathbf{x}^T\right].$$

The solution of linear system of equations can be derived using the singular value decomposition (SVD) of \mathbf{G} , which is defined as

$$\mathbf{G} = \mathbf{U} \mathbf{\Sigma} \mathbf{V}^T = \sum_{i=1}^r \sigma_i \mathbf{u}_i \mathbf{v}_i^T, \tag{5.14}$$

where Σ is a $M/2 \times M/2$ diagonal matrix with singular values $\sigma_1 \geq \sigma_2 \geq \cdots \geq \sigma_r > \sigma_{r+1} = \cdots = \sigma_p = 0$ (p = M/2 and $r \leq M/2$ is the rank of \mathbf{G} . The matrices $\mathbf{U}(M/2 \times M/2)$ and $\mathbf{V}(M/2 \times M/2)$ are formed from the columns $\{\mathbf{u}_i\}_{i=1}^{M/2}$ and $\{\mathbf{v}_i\}_{i=1}^{M/2}$, which are the orthogonal eigenvectors of $\mathbf{G}\mathbf{G}^T$ and $\mathbf{G}^T\mathbf{G}$, respectively. The solution is then given by

$$\mathbf{h} = \sum_{i=1}^{r} \frac{\mathbf{u}_{i}^{T} \mathbf{f}}{\sigma_{i}} \mathbf{v}_{i}. \tag{5.15}$$

The SVD of G forms a basis for regularization by appropriate selection of singular modes. A solution based on the constrained optimization problem, which is the general form of the regularization, can be expressed as

$$\mathbf{h}_{\text{Reg}} = \sum_{i=1}^{r} \frac{\sigma_i}{\sigma_i^2 + \gamma_i R_i^2} \mathbf{u}_i^T \mathbf{f} \mathbf{v}_i, \tag{5.16}$$

where γ_i is an appropriately chosen threshold for the *i*th singular mode and R_i^2 is quadratic ratio resulting from the quadratic kernel obtained from the *i*th singular mode.

The TSVD regularization, also known as rank reduction regularization [32], used in our previous work can be derived from Equation 5.16. When γ_i is chosen to be

$$\gamma_i = \begin{cases} 0 & , & i \le k \\ \infty & , & k < i \le r \end{cases}$$
(5.17)

where $k \leq r$ is the number of singular modes used to compute the estimate, the kth order TSVD solution is given by

$$\mathbf{h}_{\text{TSVD}}(k) = \sum_{i=1}^{k} \frac{\mathbf{u}_{i}^{T} \mathbf{f}}{\sigma_{i}} \mathbf{v}_{i}.$$
 (5.18)

5.3 Materials and Methods

In this section, the details used to identify and validate the SVF system identification algorithm are presented.

5.3.1 Details of the NPS

The NPS to be identified in Figure 5.2 consists of a linear array transducer and a synthetic phantom. The 192-element linear array is used to scan the phantom with 64 active elements and a Hanning apodization in transmit and receive. Physical descriptions of each element of the linear array are as follows: the element height is 5 mm, the width is one wavelength, and the distance between elements is 0.05 mm. In simulation, each physical element is divided into 1 by 10 mathematical element to increase accuracy. A single focus at 70 mm is used in both transmission and reception. The impulse response of the transducer is a Gaussian-modulated sinusoidal pulse with center frequency 3 MHz and fractional bandwidth 60.

The synthetic phantom is composed of scattering particles located at uniform random positions in a $20 \times 3 \times 1$ mm³ volume and Gaussian distributed scattering strengths are assigned to those particles. This phantom totally contains 166 scatterers and is centered at the focus of the transducer. An emitted field at each scattering location is passed through the temporal impulse response f_{sc} . In this paper the f_{sc} is

simulated by the SVF to generate nonlinearity. The linear kernel of the SVF is simulated using a 2-MHz Gaussian-modulated sinusoidal pulse with 85 % bandwidth. The pulse is truncated where the envelope falls 25 dB below the peak. The quadratic kernel is calculated from an outer product of the linear kernel and scaled by a constant used for controlling a nonlinearity level of the system.

5.3.2 Identification Step

In order to determine coefficients of linear and quadratic kernels, a system of linear equations (Equation 5.7) is formed using average of frequency responses resulting from 64 pseudorandom binary sequences and their corresponding outputs from the NPS. While each pseudorandom binary sequence is composed of 150 data points, each pulse-echo line from the NPS consists of 256 data points. Gaussian white noise is added to pulse-echo data to achieve the signal-to-noise ratio (SNR) of 50 and 10 dB. The identification results at SNR of 50 dB represent the case when noise level is lower than quadratic nonlinearity level. On the other hand, the identification results at SNR of 10 dB are the case when noise level is higher the quadratic nonlinearity level.

5.3.3 Validation Step

After the linear and quadratic kernels are determined, the same input is sent to both the NPS and correspondingly identified SVF system. Subsequently, outputs from those two systems are compared for validating identification results. Figure 5.4 shows a three-cycle sinusoidal pulse at 2 MHz with a Hanning weighting used in validation.

5.4 Results

5.4.1 Identification Results

In order to determine coefficients of linear and quadratic kernels, a system of linear equations (Equation 5.11) is formed using average of frequency responses resulting from 64 pseudorandom binary sequences and their corresponding outputs from the NPS.

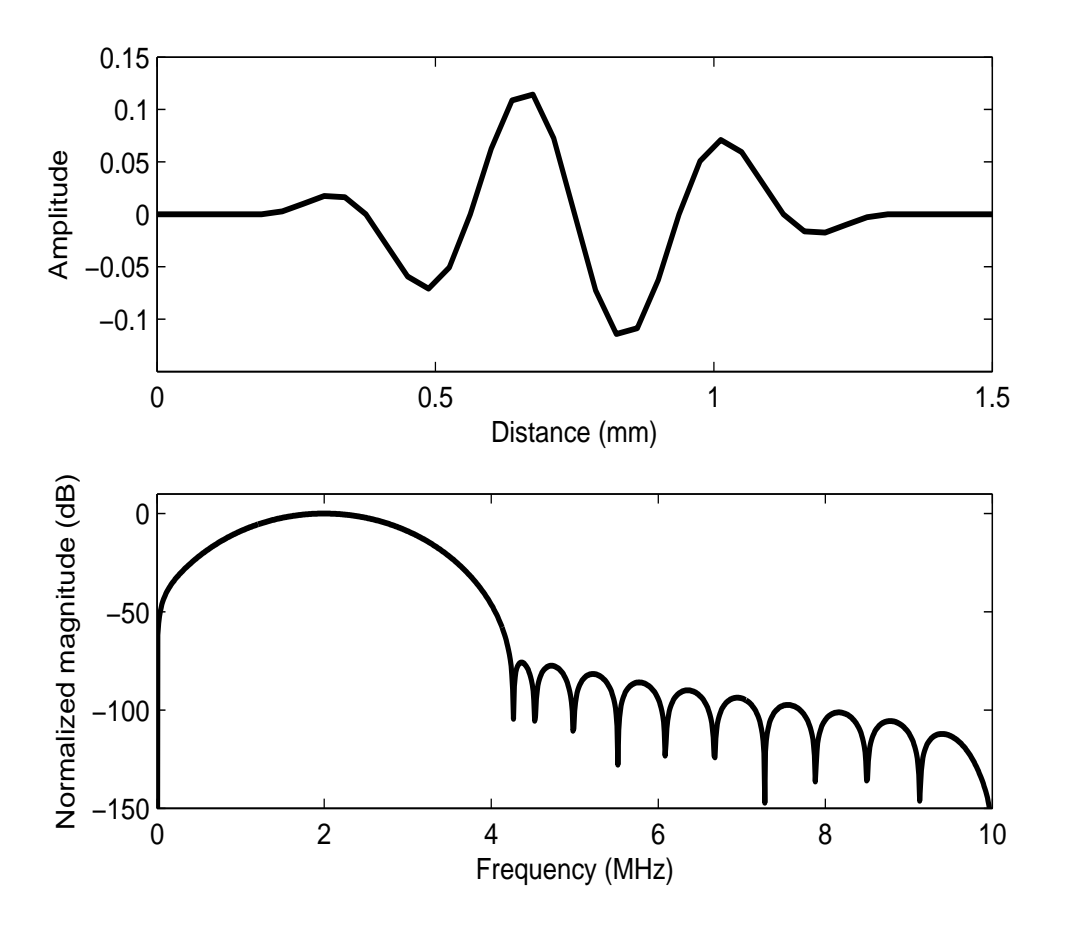


Figure 5.4: Top: A three-cycle of two-MHz sinusoidal pulse used as an input in both the NPS and SVF for validation. Bottom: The corresponding spectrum of time waveform.

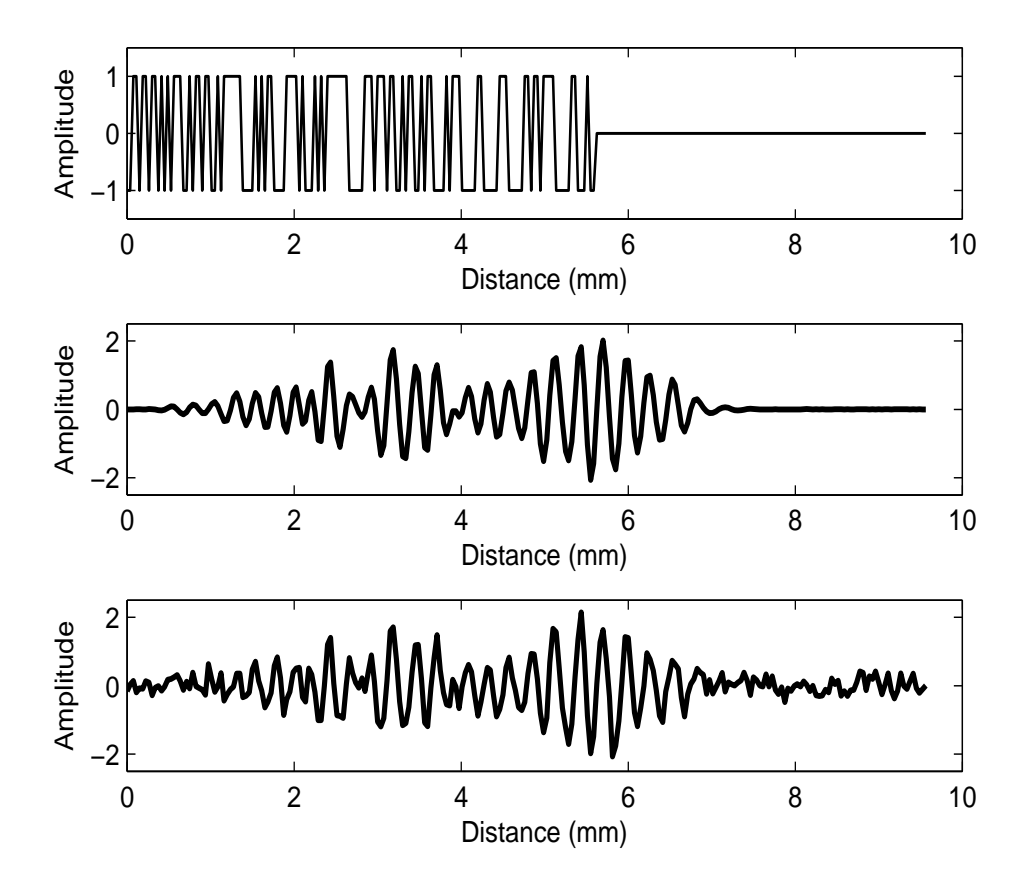


Figure 5.5: Top: Example of a pseudorandom binary sequence used as an input for the SVF identification. Middle: Corresponding time waveform from the NPS output at 50-dB SNR. Bottom: Corresponding time waveform from the NPS output at 10-dB SNR.

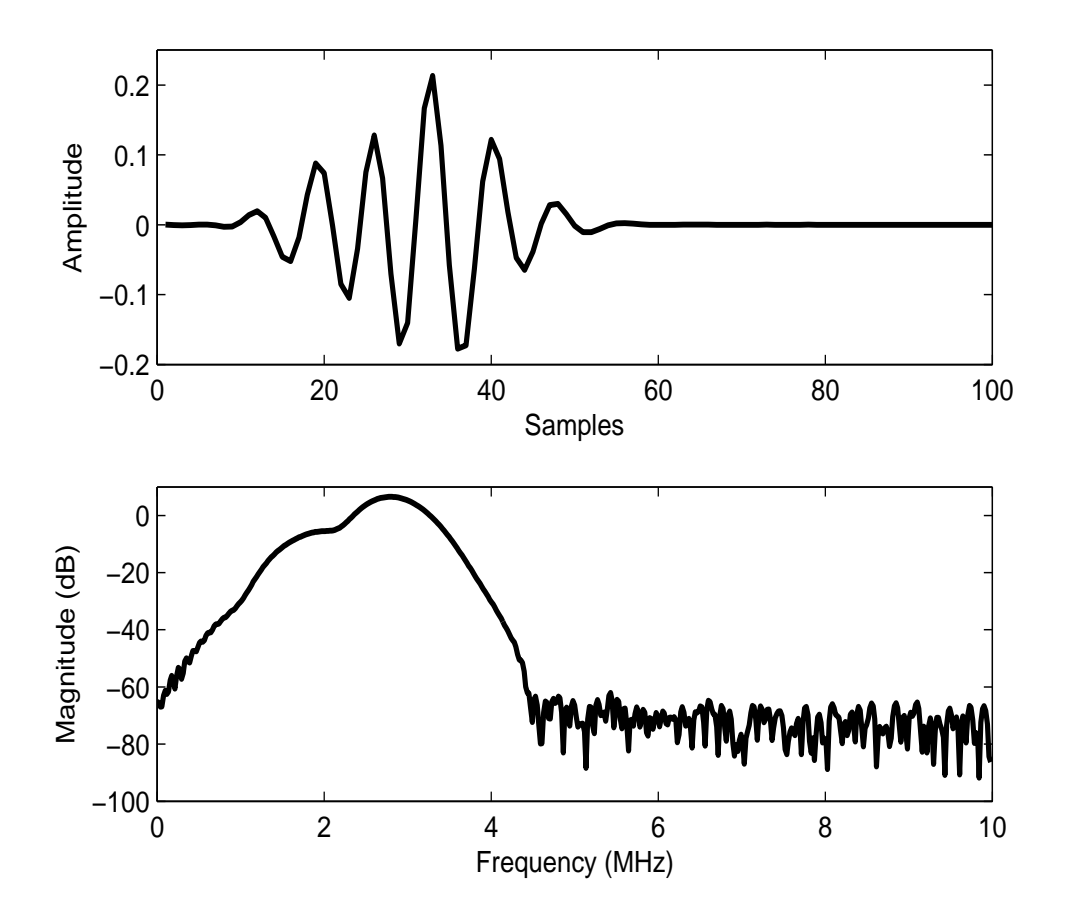


Figure 5.6: Top: Identified linear kernel in time domain. Bottom: Identified linear kernel in frequency domain.

Figure 5.5 (top) shows an example of a pseudorandom binary sequence consisting of 150 data points. The corresponding time waveforms from the NPS outputs at 50 and 10 dB are shown in middle and bottom panels, respectively.

Figure 5.6 shows the identified linear kernel in time domain in the top panel. Its corresponding magnitude frequency response is shown the bottom panel. It can be seen that the maximum of passband centered around 3 MHz, which agree with frequency characteristics of the transducer. Figure 5.7 shows the identified quadratic kernel in time domain in the left panel. Its corresponding 2D magnitude frequency response is shown the right panel. The maximum of passband centered around (2,2) and (-2,-2) MHz, whose summation corresponds to the second harmonics, i.e., 4 and -4 MHz.

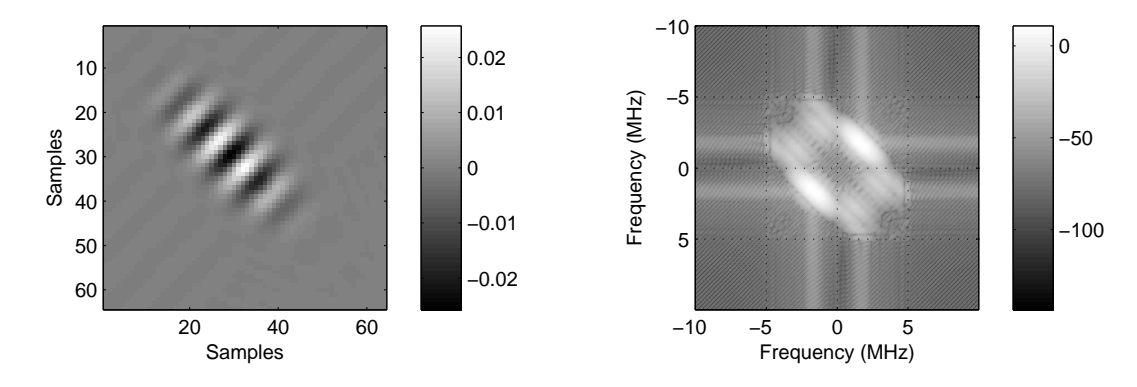


Figure 5.7: Left: Identified quadratic kernel in time domain. Right: Identified quadratic kernel in frequency domain.

5.4.2 Validation Results

Figure 5.8 shows a simulated RF line from the NPS at the SNR of 50 dB using the dotted line. The pulse duration is approximately 2.8 mm, which is longer than the transmit pulse. This is due to the fact that echoes result from multiple scatterers located within 1-mm thickness target. In addition, the corresponding spectra of time waveforms in the top panel are displayed in the bottom panel. The second harmonics is clearly observed at 4 MHz. Linear (y_L) and quadratic (y_Q) components from the SVF are shown using thin and thick lines, respectively. It can be seen that the linear kernel appropriately predicts the linear output in the fundamental energy band (around 2 MHz). On the other hand, the quadratic kernel captures energy primarily in the second harmonic and low frequency bands corresponding to second order nonlinearity covering the whole transducer bandwidth. This is the advantage of SVF approach over other static models such as linear bandpass filters whose the sensitivity to nonlinear separations is fixed to some specific frequencies, e.g. the second harmonic.

Figure 5.9 shows the identification results at the SNR of 10 dB. It can be seen that all signal components are in agreement with those from the SNR of 50 dB. It is interesting to notice that the SVF is able to extract the second order nonlinearity although its magnitude is comparable to the noise level. This is due to the fact that the

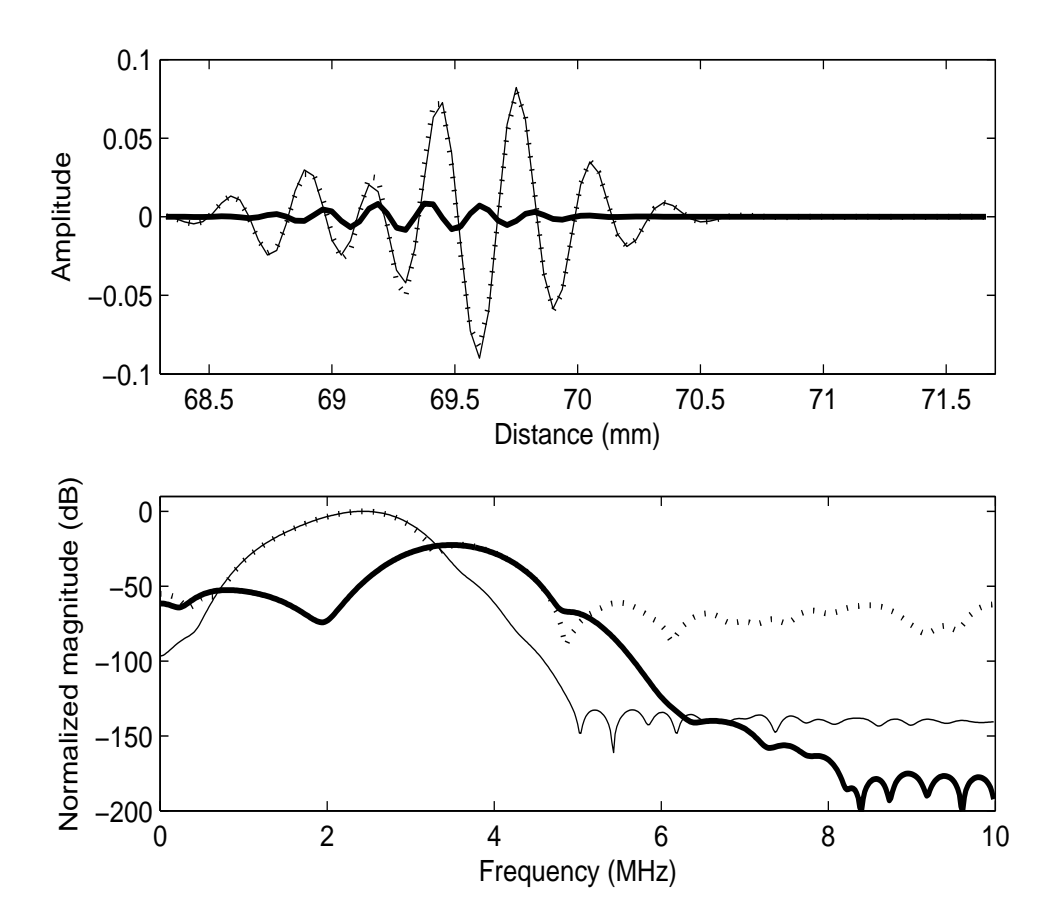


Figure 5.8: Validation results at the SNR of 50 dB. Top: Linear (thin) and quadratic (thick) components resulting from the decomposition using the SVF model compared with the NPS output (dotted). Bottom: The corresponding spectra of time waveforms in the top panel.

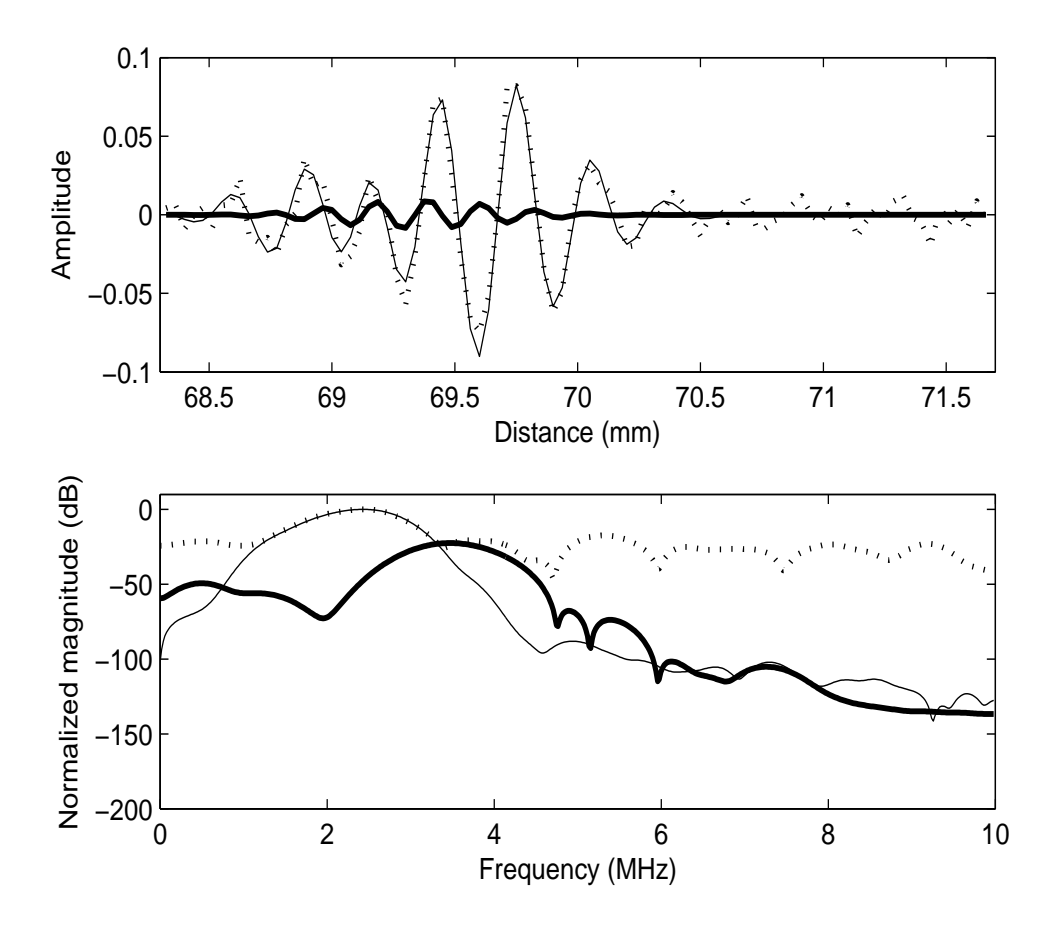


Figure 5.9: Validation results at the SNR of 10 dB. Top: Linear (thin) and quadratic (thick) components resulting from the decomposition using the SVF model compared with the NPS output (dotted). Bottom: The corresponding spectra of time waveforms in the top panel.

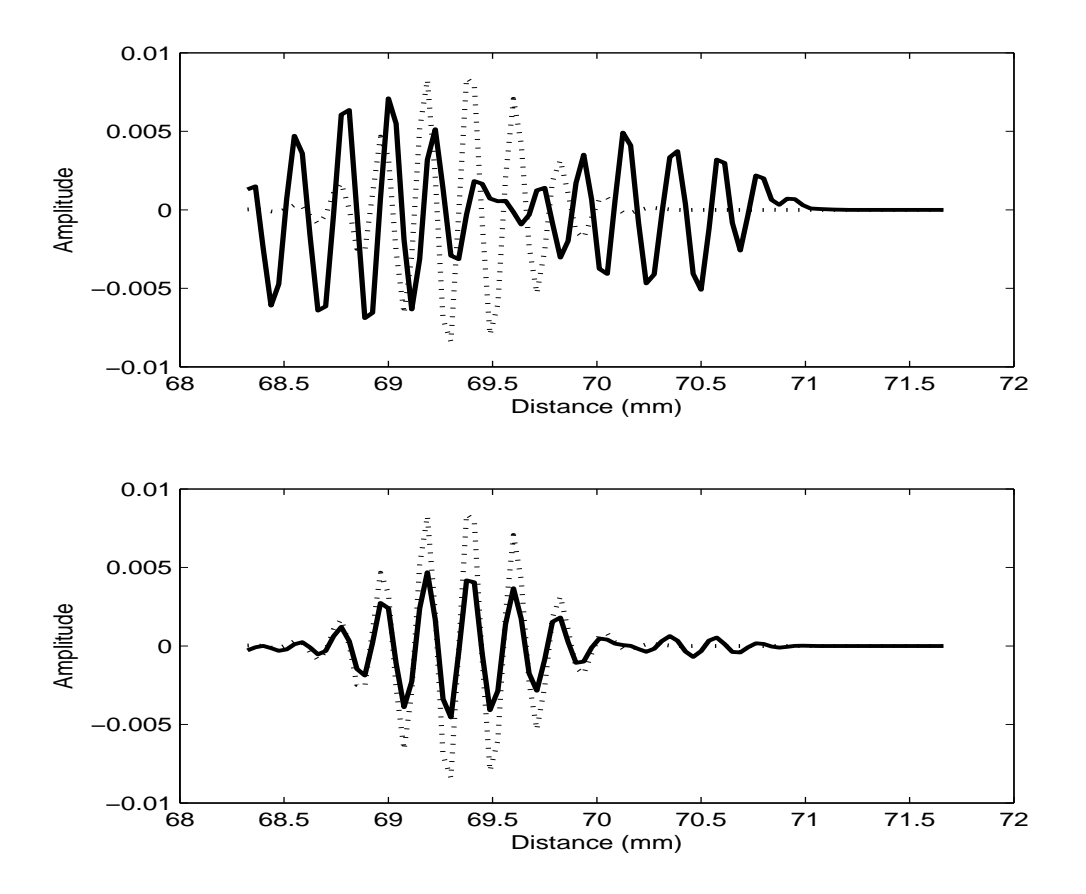


Figure 5.10: Comparisons of quadratic outputs from: (Dotted) 64 input-output sequences identification, (Solid in top panel) 16 input-output sequences identification without TSVD regularization, and (Solid in bottom panel) 16 input-output sequences identification with TSVD regularization.

system identification based on the SVF has an inherent property of robust resistance to the additive white Gaussian noise.

Figure 5.10 (top) shows comparison of quadratic output from 64 input-output sequences identification (dotted) with that from 16 input-output sequences identification without TSVD regularization (solid). Significant error can be seen. However, based on the TSVD regularization, the reduction in error of quadratic output from 16 input-output sequences is clearly shown in the bottom panel of Figure 5.10 with the solid line. This result indicates the feasibility of regularization in decreasing input-output

sequences used for system identification.

5.5 Discussion

This chapter presents the utilization of system identification based on the second-order Volterra (SVF) to separate nonlinear components of nonlinear echo signals. The algorithm for the identification of the SVF filter coefficients is validated using simulations from a nonlinear pulse-echo system. The identified linear and quadratic kernels are used to decompose the RF line from the nonlinear pulse-echo system into linear and quadratic components. Illustrative examples demonstrate that while the linear kernel appropriately captures the linear component in the fundamental frequency band, the quadratic kernel is capable of modeling quadratic components ranging from low to high frequency.

In addition, the feasibility study shows that the system identification based on the SVF is capable of separating the second order nonlinearity embedded under the level of noise signal. This is a significant advantage of the proposed method over a conventional linear filtering. Applications in practical use that the advantage of this new proposed method may allow for include medical diagnosis and tissue characterization. In the former, the proposed signal separation model can replace a linear bandpass filtering in tissue harmonic imaging (THI)[44] to obtain better images for medical diagnosis. In the latter, the acoustic nonlinearity parameter B/A [45], i.e. a measure of nonlinearity of a medium, can be obtained more efficiently using separated second harmonic in biological tissues from the proposed model. However, with this identification approach, the size of the identified Volterra kernel is dependent on the propagating distance, i.e. the phantom thickness. From a practical point of view, the Volterra kernel of the whole RF line should be determined using its small segment in order to reduce computational complexity. This issue is an ongoing investigation. Results will be reported in the future.

Chapter 6

Conclusions and Recommendations for Future Work

6.1 Conclusions

Two applications of Volterra filters for nonlinear ultrasound imaging are presented in this report. These include quadratic filter design and Volterra filter system identification. In the former, the properties of Volterra filters that affect imaging qualities both in terms of contrast and spatial resolution are analyzed. Based on the understanding in investigated properties, a novel design approach of Volterra filter for improving the quality of ultrasound images is formulated. The important finding is that the novel design approach of a quadratic filter allows for two degrees of freedom in optimizing time and frequency resolution independently. That is, axial resolution can be maintained while contrast resolution is maximized. Thus, it overcomes the trade-off in time frequency resolution problem appearing in linear bandpass filtering, which has only one degree of freedom in filter optimization. For example, in order to increase contrast resolution in linear bandpass filtering, the passband width of filter must be decreased. This unavoidably degrades axial resolution. Evaluation of the approach is demonstrated using a flow phantom target containing ultrasound contrast agent and a quality assurance ultrasound phantom consisting of resolution targets. Results show that the proposed method allows for obtaining the quadratic image with high contrast resolution and no apparent loss in axial resolution.

In the latter, a preliminary study of system identification based on Volterra filters applied in a nonlinear medical ultrasound system was carried out. System identification based on the second-order Volterra (SVF) is employed to separate nonlinear components of nonlinear echo signals. The algorithm for the identification of the SVF filter coefficients is validated using simulations from a nonlinear pulse-echo system. The identified linear and quadratic kernels are used to decompose the RF line from the nonlinear pulse-echo system into linear and quadratic components. The feasibility study shows that the system identification based on the SVF is capable of separating the second order nonlinearity embedded under the level of noise signal. This is a significant advantage of the proposed method over a conventional linear filtering. Two applications in practical use that the advantage of this new proposed method may provide include medical diagnosis and tissue characterization. For medical application, the proposed signal separation model may replace a linear bandpass filtering in tissue harmonic imaging to obtain better images for medical diagnosis. For tissue characterization, the acoustic nonlinearity parameter B/A, i.e. a measure of nonlinearity of a medium, may be obtained more efficiently using separated second harmonic in biological tissues from the proposed model.

6.2 Recommendations for Future Study

Several possible directions recommended for future study are proposed as follows:

Further Study on Quadratic Filter

The evaluation of quadratic filter design in this work was performed using only a flow phantom target containing ultrasound contrast agent and a quality assurance ultrasound phantom consisting of resolution targets. More evaluations should be explored. These include ultrasound data from *in vivo* targets, . In addition, the proposed design approach can be extended to simultaneously separate multiple harmonics for maximizing nonlinearity detection. Computational complexity reduction in quadratic filtering needs

to be further studied to make real-time implementation in modern ultrasound scanners possible.

Further Study on Volterra Filter System Identification

Based on identification approach proposed in the research, the size of the identified Volterra kernel is dependent on the propagating distance, i.e. the target thickness. From a practical point of view, the Volterra kernel of the whole RF line should be determined using its small segment in order to reduce computational complexity. Consequently, more practical identification approach need to be developed. Subsequently, the developed approach will be applied on medical ultrasound applications, e.g. ultrasound imaging enhancement and nonlinearity parameter B/A estimation.

Adaptive Volterra Filters

Adaptive forms of SVF filters are suitable for estimating local quadratic components instead of the global filtering approach. This will allow for the optimization of signal separations based on the local level of nonlinearity. Adaptive implementations of the SVF have been extensively studied in literature. Examples include the following: (1) General overviews and basic ideas of adaptive Volterra filter implementations [46]; and (2) The adaptive algorithm based on fast recursive least squares approach applicable to the second-order drift phenomena [47]. They can serve as a starting point in applying adaptive SVF filters to nonlinear imaging problems.

Higher-Order Volterra Filters

Signal components resulting from the higher-order Volterra filters (e.g., cubic) may be more sensitive to UCA nonlinearity than tissue nonlinear response. This is due to the observation that, under normal imaging conditions, tissue nonlinearity is at most quadratic. The identification of higher-order Volterra kernels based on the prediction model of Volterra filter can be easily implemented by extending the post-beamforming SVF algorithm.

Bibliography

- [1] K. V. Ramnarine, K. K. Kyriakopoulou, P. Gordon, N. W. McDicken, C. S. McArdle, and E. Leen, "Improved characterization of focal liver tumours: Dynamic power Doppler imaging using NC100100 echo-enhancer," *European Journal of Ultrasound*, vol. 11, no. 2, pp. 95–104, 2000.
- [2] C. Frischke, J. R. Lindner, K. Wei, N. C. Goodman, D. M. Skyba, and S. Kaul, "Myocardial perfusion imaging in the setting of coronary artery stenosis and acute myocardial infarction using venous injection of a second-generation echocardiographic contrast agent," *Circulation*, vol. 96, pp. 959–967, 1997.
- [3] D. Cosgrove, "Ultrasound contrast agent: An overview," European Journal of Radiology, vol. 60, pp. 324–330, 2006.
- [4] C. P. Ritz and E. J. Powers, "Estimation of nonlinear transfer functions for fully developed turbulence," *Physica 20D*, pp. 320–334, 1986.
- [5] S. W. Nam and E. J. Powers, "On the linearization of volterra nonlinear system using third-order inverses in the digital frequency-domain," in *Proc. IEEE ISCAS.*, 1990, vol. 1, pp. 407–410.
- [6] M. Tsujikawa, T. Shiozaki, Y. Kajikawa, and Y. Nomura, "Identification and elimination of second-order nonlinear distortion of loudspeaker systems using volterra filter," in *Proc. IEEE ISCAS.*, 2000, vol. 5, pp. 249–252.

- [7] A. Guerin, G. Faucon, and R. LE Bouquin-Jeannes, "Nonlinear acoustic echo cancelation based on volterra filters," *IEEE Trans. Speech Audio Processing*, vol. 11, no. 6, pp. 672–683, Nov. 2003.
- [8] R. Nowak and B. Van Veen, "Volterra filter equalization: A fixed point approach," *IEEE Tran. Signal Processing*, vol. 45, no. 2, pp. 377–388, Feb. 1997.
- [9] R. Gramiak and P. M. Shah, "Echocardiography of the aortic root," *Invest. Radiol.*, vol. 3, pp. 356–366, 1968.
- [10] F. W. Kremkau, R. Gramiak, P. M. Shah, and Kramer D. H., "Ultrasound cardio-graphy contrast studies in anatomy and function," *Radiology*, vol. 92, pp. 939–948, 1969.
- [11] F. W. Kremkau, R. Gramiak, E. L. Carstensen, P. M. Shah, and Kramer D. H., "Detection of cavitation at catheter tips," Am. J. Roentgenol. Radium. Ther. Nucl. Med., vol. 110, no. 1, pp. 177–183, 1970.
- [12] J. Ophir and K.J. Parker, "Contrast agent in diagnostic ultrasound," Ultrasond Med. Biol., vol. 15, no. 4, pp. 319–333, Nov. 1989.
- [13] S. B. Feinstein, J. Cheirif, C. F. Ten, P. R. Silverman, P. A. Heidenreich, C. Dick, and et al, "Safety and efficacy of a new transpulmonary ultrasound contrast agent: initial multicenter clinical results," J. Am. Coll. Cardiol., vol. 16, no. 2, pp. 316–324, 1990.
- [14] T Fritzsch, P. Hauff, F. Heldmann, F. Luders, V. Uhlendorf, and W. Weitschies, "Preliminary results with a new liver specific ultrasound contrast agent," *Ultra-sound Med. Biol.*, p. 20:137, 1994.
- [15] P. J. A. Frinking, A. Bouakaz, J. Kirkhorn, F. J. Ten Cate, and N. de Jong, "Ultrasound contrast imaging: current and new potential methods," *Ultrasound Med. Biol.*, vol. 26, pp. 965–975, 2000.

- [16] S. B. Feinstein, P. M. Shah, R. J. Bing, S. Meerbaum, E. Corday, B. L. Chang, G. Santillan, and et al, "Microbubble dynamics visualized in the intact capillary circulation," J. Am. Coll. Cardiol., vol. 4, pp. 595–601, 1984.
- [17] N. de Jong, F. J. Ten Cate, C. T. Lancee, J.R.T.C. Roelandt, and N. Bom, "Principles and developments in ultrasound contrast agents," *Ultrasonics*, vol. 29, pp. 324–330, Jul. 1991.
- [18] P. M. Morse and K. U. Ingard, Theoretical Acoustics, McGraw Hill, New York, 1968.
- [19] N. De Jong, "Improvement in ultrasound contrast agents," IEEE Eng. Med. Biol. Mag., vol. 15, no. 6, pp. 72–82, Nov.-Dec. 1996.
- [20] N. De Jong, R. Cornet, and C. T. Lancee, "Higher harmonics of vibrating gas filled microspheres. part one: Simulations," *Ultrasonics*, vol. 32, no. 6, pp. 447–453, 1994.
- [21] N. De Jong, R. Cornet, and C. T. Lancee, "Higher harmonics of vibrating gas filled microspheres. part two: Measurements," *Ultrasonics*, vol. 32, no. 6, pp. 455–459, 1994.
- [22] P. J. A. Frinking, N. De Jong, and E. I. Cespedes, "Scattering properties of encapsulated gas bubbles at high ultrasound pressures," J. Acoust. Soc. Am., vol. 105, no. 3, pp. 1989–1996, 1999.
- [23] M. A. Averkiou, "Tissue harmonic imaging," in Proc. IEEE Ultrason. Symp., 2000, vol. 2, pp. 1563–1572.
- [24] J. E. Chomas, P. Dayton, J. Allen, K. Morgan, and K. W. ferrara, "Mechanisms of contrast agent destruction," *IEEE Trans. Ultrason.*, Ferroelect., Freq. Contr., vol. 48, no. 1, pp. 232–248, Jan. 2001.
- [25] J. D. Kasprzak, B. Paelinck, F. J. Ten Cate, W. B. Vletter, N. de Jong, D. Pold-ermans, A. Elhendy, A. Bouakaz, and J. R. Roelandt, "Comparison of native and

- contrast-enhanced harmonic echocardiography for visualization of left ventricular endocardial border," Am. J. Cardiol., vol. 83, no. 2, pp. 211–217, 1999.
- [26] S. Kaul and R. Jayaweera, "Coronary and myocardium blood volumes: Noninvasive tools to assess the coronary microcirculation," *Circulation*, vol. 96, pp. 719–724, 1997.
- [27] P. J. A. Frinking, E. Cespedes, J. Kirkhorn, H. Torp, and N. de Jong, "A new contrast ultrasound imaging approach based on the combination of multiple imaging pulses and a separate release burst," *IEEE Trans. Ultrason.*, Ferroelect., Freq. Contr., vol. 48, no. 3, pp. 643–651, May. 2001.
- [28] D. H. Simpson, C. T. Chin, and P. N. Burns, "Pulse inversion doppler: A new method for detecting nonlinear echoes from microbubble contrast agent.," *IEEE Trans. Ultrason.*, Ferroelect., Freq. Contr., vol. 46, no. 2, pp. 372–382, Mar. 1999.
- [29] D. H. Simson and C. T. Chin, "Perfusion imaging with pulse inversion doppler and microbubble contrast agents: in vivo studies of the myocardium," in *Proc. IEEE Ultrason. Symp.*, 1998, vol. 2, pp. 1784–1786.
- [30] H. Yao, P. Phukpattaranont, and E. S. Ebbini, "Post-beamforming second-order volterra filter for nonlinear pulse-echo imaging," in *Proc. ICASSP.*, 2002, vol. 2, pp. 1133–1136.
- [31] G. H. Golub and C.F. Van Loan, Matrix Computations, Johns Hopkins University Press, Baltimore, MD, 2nd edition, 1989.
- [32] J. Shen and E. S. Ebbini, "A new coded excitation ultrasound imaging system: Part I-Basic principles," *IEEE Trans. Ultrason.*, Ferroelect., Freq. Contr., vol. 43, no. 2, pp. 131–140, 1996.

- [33] P. Phukpattaranont and E. S. Ebbini, "Post-beamforming Volterra filters for contrast-assisted ultrasonic imaging: in-vivo results," in Proc. IEEE Ultrason. Symp., 2003, vol. 2, pp. 1191–1194.
- [34] P. Phukpattaranont and K. Chetpattananondh, "Post-beamforming second-order volterra filters for contrast agent imaging: A frequency-domain aspect," in *Proc. Symp. Ultrasonic Electronics*, 2005, pp. 281–282.
- [35] P. Phukpattaranont, T. Nilmanee, C. Limsakul, and E. S. Ebbini, "Design of quadratic filters for contrast-assisted ultrasonic imaging," in *Proc. IEEE Ultrason.* Symp., 2007, pp. 2211–2214.
- [36] W. P. Zhu, M. O. Ahmad, and M. N. S. Swamy, "A least-square design approach for 2-d fir filters with arbitrary frequency response," *IEEE Trans. Circuits Syst. II*, vol. 46, no. 8, pp. 1027–1034, 1999.
- [37] J. fang and L. E. Atlas, "Quadratic detectors for energy estimation," IEEE Trans. Signal Processing, vol. 43, no. 11, pp. 2582–2594, 1995.
- [38] P. Phukpattaranont and E. S. Ebbini, "Post-beamforming second-order volterra filter for pulse-echo ultrasonic imaging," *IEEE Trans. Ultrason.*, Ferroelect., Freq. Contr., vol. 50, no. 8, pp. 987–1001, Aug. 2003.
- [39] J. A. Jensen and N. B. Svendsen, "Calculation of pressure fields from arbitrarity shaped, apodized, and excited ultrasound transducers," *IEEE Trans. Ultrason.*, Ferroelect., Freq. Contr., vol. 39, no. 2, pp. 262–267, Mar. 1992.
- [40] M. E. Frijlink, D. E. Goertz, A. Bouakaz, and A. F. W. van der Steen, "Intravascular ultrasound tissue harmonic imaging: A simulation study," *Ultrasonics*, vol. 44, pp. 185–188, 2006.
- [41] K. E. Morgan, J. S. Allen, P. A. Dayton, J. E. Chomas, A. L. Klibanov, and K. W. Ferrara, "Experimental and theoretical evaluation of microbubble behavior: Effect

- of transmitted phase and bubble size," *IEEE Trans. Ultrason.*, Ferroelect., Freq. Contr., vol. 47, no. 6, pp. 1494–1509, Nov. 2000.
- [42] G. L. Sicuranza, "Quadratic filters for signal processing," Proc. of the IEEE, vol. 80, no. 8, pp. 1263–1285, Aug. 1992.
- [43] K. I. Kim and E. J. Powers, "A digital method of modeling quadratically nonlinear systems with a genearal random input," *IEEE Trans. Acoust., Speech, Signal Processing*, vol. 36, no. 11, pp. 1758–1769, Nov. 1988.
- [44] D. Zhang, X. Gong, and X. Chen, "Experimental imaging of the acoustic nonlinearity parameter B/A for biological tissues via a parametric array," *Ultrasound Med. Biol.*, vol. 27, no. 10, pp. 1359–1365, 2001.
- [45] V. F. Humphrey, "Nonlinear propagation in ultrasonic fields: measurements, modelling and harmonic imaging," *Ultrasonics*, vol. 38, no. 1-8, pp. 267–272, 2000.
- [46] V. J. Mathews, "Adaptive polynomial filters," IEEE SP Magazine, vol. 8, no. 3, pp. 10–26, Juln. 1991.
- [47] K. Kim, S. B. Kim, E. J. Powers, R. W. Miksad, and F. J. Fischer, "Adaptive second-order volterra filtering and its application to second-order drift phenomena," *IEEE J. Oceanic Eng.*, vol. 19, no. 2, pp. 183–192, Apr. 1994.

Subject: Acceptance of your paper for JJAP (UE08140)

From: "JJAP_special" <jjap_special@ipap.jp>

Date: Thu, June 4, 2009 2:42 pm

To: pornchai.p@psu.ac.th

Dear Dr. Pornchai Phukpattaranont,

We are pleased to be able to inform you that your paper has been accepted for publication in Japanese Journal of Applied Physics as indicated below. We will provide you the proof sheets of the paper and the form of the publication charge certification in PDF format on our web site during a period below.

[Note] "Acrobat reader" (Adobe free software) is essential to view PDF format file. As we will send you notification e-mail when these PDF files are available, please download and print the documents, and return them to us with your corrections via fax or e-mail within 3 days excluding holidays.

Please let us know if you are not able to access Internet during the period.

Sincerely yours,

Editor-in-Chief Japanese Journal of Applied Physics

.....

Type of paper: RP

Manuscript No.: UE08140

Title: Optimum Quadratic Filters for Nonlinear Ultrasonic Imaging

Authors: Pornchai Phukpattaranont, Chusak Limsakul

Received date: 2008/11/19 Accepted date: 2009/02/02

Revised date:

Publication issue (scheduled): vol. 48 no. 7

Notification e-mail will be sent to: pornchai.p@psu.ac.th

PDF Proof will be available during: <09/06/10> and <09/06/12> Reprint of the paper will be shipped to: Pornchai Phukpattaranont

Department of Electrical Engineering, Prince of Songkla University

90112 Department of Electrical Engineering, Prince of Songkla

University, Hat Yai, Songkhla

Others-Thailand

Please indicate the correct shipping address in the form of the publication charge certification if you need to change from the address above.

JJAP Editorial Division

Institute of Pure and Applied Physics

2-31-22-5F, Yushima, Bunkyo-ku, Tokyo 113-0034, Japan

TEL: +81-3-5844-3291 FAX: +81-3-5844-3290 URL: http://jjap.ipap.jp Subject: Acceptance of your paper for JJAP (UE08141)

From: "JJAP_special" <jjap_special@ipap.jp>

Date: Thu, June 4, 2009 2:42 pm

To: pornchai.p@psu.ac.th

Dear Dr. Pornchai Phukpattaranont,

We are pleased to be able to inform you that your paper has been accepted for publication in Japanese Journal of Applied Physics as indicated below. We will provide you the proof sheets of the paper and the form of the publication charge certification in PDF format on our web site during a period below.

[Note] "Acrobat reader" (Adobe free software) is essential to view PDF format file. As we will send you notification e-mail when these PDF files are available, please download and print the documents, and return them to us with your corrections via fax or e-mail within 3 days excluding holidays.

Please let us know if you are not able to access Internet during the period.

Sincerely yours,

Editor-in-Chief

Japanese Journal of Applied Physics

.....

Type of paper: RP

Manuscript No.: UE08141

Title: Separation of Nonlinear Ultrasound Signals Based on Second-Order

Volterra System Identification Authors: Pornchai Phukpattaranont

Received date: 2008/11/19 Accepted date: 2009/03/22

Revised date:

Publication issue (scheduled): vol. 48 no. 7

Notification e-mail will be sent to: pornchai.p@psu.ac.th

PDF Proof will be available during: <09/06/10> and <09/06/12> Reprint of the paper will be shipped to: Pornchai Phukpattaranont Department of Electrical Engineering, Prince of Songkla University

90112 Department of Electrical Engineering, Prince of Songkla

University, Hat Yai, Songkhla

Others-Thailand

Please indicate the correct shipping address in the form of the publication charge certification if you need to change from the address above.

JJAP Editorial Division

Institute of Pure and Applied Physics

2-31-22-5F, Yushima, Bunkyo-ku, Tokyo 113-0034, Japan

TEL: +81-3-5844-3291 FAX: +81-3-5844-3290 URL: http://jjap.ipap.jp